

## THE BOLOCAM GALACTIC PLANE SURVEY: SURVEY DESCRIPTION AND DATA REDUCTION

JAMES AGUIRRE<sup>1</sup>, ADAM GINSBURG<sup>2</sup>, MIRANDA K. NORDHAUS<sup>3</sup>, MEREDITH DROSBACK<sup>4</sup>, JOHN BALLY<sup>2</sup>, CARA BATTERSBY<sup>2</sup>, ERIC TODD BRADLEY<sup>5</sup>, CLAUDIA CYGANOWSKI<sup>6</sup>, DARREN DOWELL<sup>7</sup>, NEAL J. EVANS II<sup>3</sup>, JASON GLENN<sup>2</sup>, PAUL HARVEY<sup>3,2</sup>, ERIK ROSOLOWSKY<sup>8</sup>, GUY S. STRINGFELLOW<sup>2</sup>, JOSH WALAWENDER<sup>9</sup>, AND JONATHAN WILLIAMS<sup>10</sup>

<sup>1</sup>Department of Physics and Astronomy, University of Pennsylvania, Philadelphia, PA

<sup>2</sup>CASA, University of Colorado, CB 389-UCB, Boulder, CO 80309

<sup>3</sup>Department of Astronomy, University of Texas, 1 University Station C1400, Austin, TX 78712

<sup>4</sup>Department of Astronomy, University of Virginia, P.O. Box 400325, Charlottesville, VA 22904

<sup>5</sup>Department of Physics, University of Central Florida

<sup>6</sup>Department of Astronomy, University of Wisconsin, Madison, WI 53706

<sup>7</sup>Jet Propulsion Laboratory, California Institute of Technology, 4800 Oak Grove Dr., Pasadena, CA 91104

<sup>8</sup>Department of Physics and Astronomy, University of British Columbia, Okanagan

<sup>9</sup>Institute for Astronomy, University of Hawaii, 640 N. Aohoku Pl., Hilo, HI 96720 and

<sup>10</sup>Institute for Astronomy, University of Hawaii, 680 Woodlawn Drive, Honolulu, HI 96822

DRAFT: 14:57 EDT Monday 4May 2009

### ABSTRACT

We present the Bolocam Galactic Plane Survey (BGPS), a 1.1 mm continuum survey of 150 square degrees of the Galactic Plane with 130 in the 1st quadrant, 31 in the 2nd, and 6 in the 3rd. The BGPS represents the first large area, systematic survey of the Northern Galactic Plane in the millimeter continuum without pre-selected targets. The survey has detected 7628 clumps to a limiting non-uniform 1- $\sigma$  noise level in the range 20 and 50 mJy beam<sup>-1</sup>RMS. We present maps of 97 contiguous square degrees from  $l = -10.5$  to  $l = 86.5$  and  $b = \pm 0.5$  with a resolution of  $\sim 33''$ , as well as regions in IC1396,  $l = 111$  (NGC7538), W3/4/5, and Gem OB1. The most striking feature of the maps is the filamentary structure of millimeter emission throughout the Galaxy.

This paper details the survey observations and methods. We treat carefully the determination of pointing and flux density calibration errors and compare our results to the literature. Data processing algorithms that separate astronomical signals from time-variable atmospheric flux density in the data time-stream are discussed. The algorithms reproduce the structure of the astronomical sky on a *limited range of angular scales* and produce artifacts in the vicinity of bright sources. Specifically, extended emission smooth on scales larger than about 3' is not fully recovered in the images. The spatial frequency response function of the Bolocam Galactic Plane Survey is discussed.

This paper serves as a companion and guide to the public data release through NASA's Infrared Processing and Analysis Center (IPAC). These images represent an important finder chart for future observations with ALMA and a long-wavelength spectral band complementary to ATLASGAL and imminent submillimeter surveys with SCUBA-2 and Herschel-SPIRE.

*Subject headings:* ISM: - molecular clouds – stars: formation – high mass millimeter continuum

### 1. INTRODUCTION

Millimeter-wavelength continuum surveys of the Galactic plane provide the most efficient way to find molecular clumps that are the likely sites of formation for massive stars and star clusters. The development of detector arrays has made blind surveys of large areas possible. Such surveys bypass the need for selection based on the presence of embedded stars or star clusters, infrared sources, masers, or radio continuum emission. In particular, they can locate molecular clumps before stars form, providing vital information on the initial conditions of star formation. These surveys can also provide valuable constraints on the physical properties of the clumps, especially masses and mean densities, in conjunc-

tion with distance information.

Galaxy-wide surveys are essential for measuring the impacts of the environment on clump properties and star formation activity. Do clump properties vary with Galactocentric distance, or with location with respect to spiral arms? Do they depend on the level of nearby star formation activity? Answering these questions in our Galaxy will provide the essential "ground truth" required for the analysis of distant galaxies where individual clouds and clumps are not resolved and only galaxy-wide average quantities can be measured.

Surveys of the galaxy in CO line emission (Dame et al. 2001; Jackson et al. 2006) have identified the locations of large molecular clouds and traced the transition from atomic gas in the outer galaxy to molecular gas in the inner galaxy. Together with

kinematic distances (e.g. Pohl et al. 2008) and, more recently, accurate distances from VLBI (Reid et al. 2009), these surveys have begun to reveal the spiral structure of the Milky Way. As this picture comes into sharper focus, we can begin to address the old question of the relationship between spiral density waves and star formation.

To pursue this question, we need tracers of higher density material. Studies of nearby clouds have demonstrated that star formation is far from uniform over molecular clouds, but is concentrated in unusually dense regions called clumps or cores, which fill a small fraction of the area of most clouds (Lada et al. 1991; Enoch et al. 2007; Evans et al. 2009). Following Williams et al. (2000) and McKee & Ostriker (2007), we use the term ‘core’ to refer to a very dense region destined to form an individual star or small multiple star system and the term ‘clump’ to refer to a region likely to form a group or cluster of stars. While clumps forming massive clusters may be even denser than cores forming low mass stars (Mueller et al. 2002), in general, clumps are larger and have a lower mean density (McKee & Ostriker 2007). Clumps can be traced with line emission from molecules such as NH<sub>3</sub>, H<sub>2</sub>CO, CS, HCN, etc. Spectral lines also provide excellent diagnostics of line-of-sight motions, temperatures, and densities. However, the interpretation of these gas tracers is complicated by variations in tracer abundances caused by freeze-out onto grains, sublimation caused by star formation, and subsequent complex chemical processing (van Dishoeck & Blake 1998). Interpretation is further complicate by uncertainties in optical depths and excitation conditions and the impacts of radiation fields and shocks. These complications make the derivation of column densities, masses, and other physical properties of star-forming clumps very difficult. A limitation of spectral line surveys is that the tracers of denser gas tend to be weak and multi-element receiver arrays have only a modest number of elements, making blind surveys very time-consuming. Consequently, no blind surveys of the Galaxy have been done in lines that trace the molecular clumps.

In contrast, focal-plane arrays containing hundreds of individual bolometers sensitive to millimeter and sub-millimeter (sub-mm) radiation are now available. This advance in technology enables blind surveys of the Galactic plane, providing a uniform inventory of massive star-forming and starless clumps. Catalogs resulting from these surveys will provide the data base for subsequent observations in tracers such as hard-to-excite molecular lines and higher resolution studies with instruments like CARMA and ALMA. A significant advantage of continuum observations of dust at long wavelengths is the low optical depth of the dust (Johnstone & Bally 2006), permitting a straight-forward estimate of the mass of the emitting region.

Submillimeter observations of Galactic sources have been conducted by a variety of different groups

focusing on small regions. The Submillimeter Common-User Bolometer Array (SCUBA) on the 15-m James Clerk Maxwell Telescope mapped many significant regions in the galactic plane over its 8 year lifetime (Holland et al. 1999; Di Francesco et al. 2008), but never completed a contiguous survey of the galactic plane. The Bolocam instrument has been used on the 10.4-m Caltech Submillimeter Observatory (CSO) to map nearby large molecular clouds at 1.1 mm and identify hundreds of cores (Enoch et al. 2006). MAMBO on the 30-m IRAM telescope has been used at 1.2 mm to map both small, nearby cores (Kauffmann et al. 2008) and more distant regions of more massive star formation (Motte et al. 2007). None of these surveys covered a significant fraction of the Galactic plane.

Two large surveys of the Galactic plane are in progress. The ATLASGAL survey, using the LABOCA instrument at 870  $\mu\text{m}$  with 12'' resolution on the APEX telescope in Chile, will cover the southern Galactic plane and some of the north. Initial results from this survey have been reported by Schuller et al. (2009). The overlap region between BGPS and ATLASGAL is in the region  $-10.5 < l < 11.5$  and  $15 < b < 21$ ,  $-0.5 < b < 0.5$ , though ATLASGAL will eventually expand up to  $l = 60$ . The two surveys provide complementary samples of the long-wavelength end of the spectral energy distribution in Galactic star forming regions.

This paper presents the results of the Bolocam Galactic Plane Survey (BGPS). The survey covers the contiguous range  $-10.5 < l < 86.5$ ,  $-0.5 < b < 0.5$  with additional coverage to higher  $|b|$  in the range  $77 < l < 86.5$  and in the  $l = 111$ , W3/4/5, Gem OB1, and IC 1396 regions. It is complementary to the survey by Schuller et al. (2009) in that it targets the part of the plane visible from the northern hemisphere and uses a somewhat longer wavelength, allowing comparison of properties in the region of overlap with the ATLASGAL survey. In addition, the BGPS covers the Galactic anti-center region, allowing consistent comparison of very different parts of the Galaxy. At 870  $\mu\text{m}$ ,  $h\nu/k = 16.5$  K, compared to 13.1 K at 1.1 mm. Because starless clumps may be quite cold ( $T_D \approx 10$  K), the uncertainty in mass caused by uncertain temperature is slightly less at 1.1 mm. For example, if the actual  $T_D = 20$  K, rather than 10 K, the mass estimate would decrease by a factor of 3.3 at 870  $\mu\text{m}$  versus a factor of 2.9 at 1.1 mm. In addition, the Bolocam bandpass excludes the CO  $J = 2 \rightarrow 1$  line, which can be a significant contaminant on top of the dust continuum emission.

We have used the 144-element Bolocam focal plane array, mounted at the Cassegrain focus of the CSO, to survey over 150 square degrees of the northern Galactic plane at a wavelength of 1.1 mm in the dust continuum. Figure 1 shows the coverage of the BGPS. We have detected 7628 clumps in the surveyed fields, providing a sample of clumps suitable for multi-wavelength and high-resolution

studies with existing telescopes and future facilities. This sample is free of the usual biases associated with observing only regions with signposts of star formation, such as HII regions or masers. While sensitivity limits will bias the survey against distant, low-mass objects, follow-up studies indicate that many sources are more massive, distant objects (Bally et al. 2009; Nordhaus et al. 2009; Rosolowsky et al. 2009). These objects are likely to be aggregates of star forming cores found in a larger molecular cloud environment, which we will refer to as clumps (Williams et al. 2000). The clump catalog is described in a companion paper (Rosolowsky et al. 2009).

The outline of the paper is as follows. Section 2 describes the instrument and the observations. Section 3 briefly describes the data reduction process, while Sections 4 to 9 provide greater detail on flux calibration, astrometry, the mapping algorithm, noise, photometry, and the public data release. We conclude in Section 10 with brief discussion of the immediate implications of the emission revealed by the BGPS.

## 2. OBSERVATIONS

Bolocam<sup>1</sup> is the facility 144-element bolometer array camera operating on the 10.4 m dish of the Caltech Submillimeter Observatory (CSO) on the summit of Mauna Kea. We used the filter configuration with a bandcenter of 268 GHz (hereafter 1.1 mm) and fractional bandwidth  $\Delta\nu/\nu = 0.17$  (45.5 GHz). The passband is constructed to exclude the  $^{12}\text{CO}(2 \rightarrow 1)$  emission line. Figure 2 shows the passband. We compute color corrections in Appendix A.

The array field-of-view is 7'.5, with individual detectors having nearly Gaussian beams of 33'' FWHM. The spacing of the pixels at 1.1 mm is  $1.6f\lambda$ , so the focal plane is not instantaneously sampled. The Bolocam instrument is described in greater detail in Haig et al. (2004) and Glenn et al. (2003).

The maps presented here were acquired during six separate observing sessions at the CSO over the course of two years. The observing epochs are given in Table 4, along with corresponding ranges for the zenith opacity  $\tau_{225}$  of the CSO tipper tau. Bolocam observations were typically scheduled when  $\tau_{225} > 0.06$ . Between observing epochs, Bolocam was removed from its mount at the re-imaged Cassegrain focus and stored warm. Thus the flux calibration and pointing model must be re-computed for each epoch to allow for variations in the instrument and optics. We found that the flux calibration did not in fact differ significantly between epochs. We observed additional pointing sources during Epoch V and therefore used it as the master pointing model.

Our basic observing strategy was to raster scan Bolocam by moving the primary mirror of the CSO

to modulate the astrophysical signal faster than fluctuations in atmospheric opacity. Each field was scanned with alternating raster scans along  $l$  and  $b$ . In Epoch I-II, the fundamental scan unit was a  $1^\circ \times 1^\circ$  block, scanned 23 times in  $l$  and  $b$ . Starting with Epoch III, the fundamental scan unit was changed to a  $3^\circ \times 1^\circ$  block for increased mapping efficiency. Each block was scanned with 23 scans along lines of constant  $b$ , and 67 scans along lines of constant  $l$ . In both cases, the spacing between adjacent rasters was 162''. The total time for such a scan was 39 (48) minutes for the  $b$  ( $l$ ) scans. The data were electronically sampled at 10 Hz along the scan direction, slightly higher than the Nyquist rate for the scan speed of  $120'' \text{ s}^{-1}$ .

In order to fill in the instantaneously undersampled focal plane, we began using in Epoch II a field rotator to mechanically align the focal plane at an optimal orientation along the scan direction to improve the sampling orthogonal to the scan direction. This is shown in Figure 3. Achieving good sampling is complicated by a number of missing bolometers. A simulation was performed to determine the optimal angle to rotate the array with respect to the scan direction to account for the beam spacing and missing bolometers. During the turnaround following a raster, the field rotator is adjusted to this optimum angle. Without the field rotator, the coverage shows variations of 100% from pixel to pixel in a single raster of a field. With the rotator, this is reduced to  $\sim 40\%$ .

## 3. OVERVIEW OF THE DATA REDUCTION

A number of different descriptions of the reduction of Bolocam data have been published (Laurent et al. 2005; Enoch et al. 2006; Sayers et al. 2009b). This work addresses the issues specific to the BGPS, significantly improving the method of Enoch et al. (2006) for generating maps and characterizing their properties and is similar in many respects to the methods presented in Cotton et al. (2009) or Kovács (2008). It incorporates some of the technical developments of Sayers et al. (2009b), though the exquisite control of systematics and noise of that analysis is neither necessary nor possible here.

The data were reduced with a custom pipeline written specifically for the BGPS. A key element of the reduction is the iterative estimation of the atmospheric fluctuations and the astrophysical signal. The atmospheric model is developed from a set of principal components of the bolometer signal time series under the assumption that the bulk of the correlated signal is atmospheric (under this assumption, astrophysical extended structures are treated as atmospheric noise). The iterative estimation process then helps to restore correlated flux due to astrophysical emission (Section 6).

The Bolocam observations are sensitive to structure between 33'' and about 200'' (half the array field of view, see figure 19). We present a detailed analysis of the filter function in our survey in figure

<sup>1</sup> <http://www.cso.caltech.edu/bolocam>

19. The data were sampled onto a uniform  $7''/2$  grid. Flux density calibrations were performed using observations of Mars and Uranus, and the overall calibration accuracy is estimated to be  $\sim 15\%$ . The flux calibration is described in section 4.

Noise properties across the survey are not completely uniform, but the measured  $1\sigma$  level is  $\approx 43 \pm 7$  mJy beam $^{-1}$  within the  $b = \pm .5$  portion of the plane in the 1st quadrant.

A separate model was constructed for each epoch, but epoch V was used as the primary pointing calibration and is shown in figure 8. In epoch V and VI, pointing sources were observed more frequently to obtain a better-constrained master pointing model. The absolute pointing accuracy was  $\sim 6''$  RMS. The Epoch V pointing model was used to make pointing reference fields to which all other fields were aligned using a cross-correlation algorithm (Section 5).

Bright and large sources leave an impact on their surroundings when cleaned with a principal component subtraction. Sgr B2, G 34.3+0.15, and other sources with fluxes  $\geq 10$  Jy are surrounded by substantial negative bowls. Some flux is restored in these bowls using the iterative process, but around the brightest sources the impact of the source on the background estimation is too great to be fully recovered (Section 8).

Instrument glitches and cosmic ray hits have been removed by a combination of outlier rejection in each spatial pixel and hand flagging of the timestream data. Streaking in the images results from incorrect determinations of the zero level across scans when a bright source is encountered and variable noise in each strip from variable dwell time. Atmospheric noise in observations taken in poor weather may not be completely removed by the reduction procedures because the atmospheric opacity can vary over timescales comparable to the time to scan astrophysical sources (Section 7).

#### 4. FLUX DENSITY AND SURFACE BRIGHTNESS CALIBRATION

The absolute flux calibration is derived from observations of Mars and Uranus (the “primary calibrators”). The millimeter-wave flux of these planets is known to  $\sim 5\%$  (Orton et al. 1986; Griffin & Orton 1993). Calibrations at (sub)millimeter wavelengths are strongly affected by atmospheric opacity corrections. Further, the detector responsivity of Bolocam’s bolometers is a non-linear function of the mean atmospheric loading.

To relate observations of the primary calibrators to observations of the BGPS fields, we make use of the following relation. The calibration  $\mathcal{S}$ , referenced to the detectors, is given by

$$\mathcal{S} \left[ \frac{\text{V}}{\text{Jy}} \right] = S(\tau) \eta A \exp(-\tau) \Delta\nu \quad (1)$$

where  $S$  is the bolometer responsivity ([V/W]),  $\eta$  is the system optical efficiency,  $A$  is the effective telescope collecting area,  $\Delta\nu$  is the bandwidth, and  $\tau$  is

the line-of-sight, in-band atmosphere opacity. Under the assumption that the only power variation on the detectors is due to the power from the atmosphere (i.e. that astronomical sources are faint relative to the atmosphere), which may be parameterized by  $\tau$ ,  $\mathcal{S}$  is a single-valued function of  $\tau$ . We have used the mean bolometer resistance as a proxy for  $\tau$ , since the bolometer resistance is a single-valued function of loading. *This quantity is monitored continuously for all observations.* Note that this calibration curve folds in both the effects of changing atmospheric transmission and the changes in the detector response with optical loading.

A fit to the observed values (measured potential difference vs. known flux density) for the primary calibrators was performed for each epoch separately. The agreement between epochs was good, so a single combined calibration was used for all data. The calibration curve is shown in Figure 4. The resulting error on the calibration curve fit is less than 5% (statistical) over the observed range of  $\tau$ . A tally of all contributions to the flux density error is given in Table 5.

The above flux density calibration only accounts for the average calibration of bolometer Volts to Janskys. It is also necessary to account for the variation of bolometer response across the focal plane. We do this by monitoring the response to the atmosphere emission in all bolometers (astrophysical signal is negligible except at SgrB2). Being in the near field, the atmosphere is common to all detectors, and thus this serves as a common relative reference to calibrate out variation in the individual detector responsivities and optical efficiencies. The properties of atmospheric noise above Mauna Kea as inferred from the Bolocam data are discussed in Sayers et al. (2009a). The change in relative response with loading for a typical detector is shown in Figure 4. The actual application of the method to the time series of the bolometer data is shown in Figure 5, where it is clear that correlation of the timestreams is indeed improved by the application of a single multiplicative factor. The implementation of this calibration in the context of the larger mapping algorithm is discussed further in Section 6.

The instrument beam size (PSF) is measured using the planets Uranus and Neptune which are nearly point sources for Bolocam. The maps of the planets, including all detectors, are fit to a Gaussian profile. The beam area is that averaged over all detectors, and is  $1.71 \times 10^{-6}$  steradians ( $33''$ ). This allows conversion of the maps, calibrated in Jy beam $^{-1}$ , into surface brightness (MJy sr $^{-1}$ ). The uncertainty in the mean beam size is 3%, leading to a corresponding additional uncertainty in the surface brightness calibration.

##### 4.1. Comparison to Other Surveys

Comparison of the BGPS flux density calibration with SCUBA 850  $\mu\text{m}$  or ATLASGAL 870  $\mu\text{m}$  results is complicated by the poorly determined variations

in the dust spectral index produced by emissivity variations. However, there are several large-area surveys with the IRAM 30 meter telescope at 1.2 mm which can be used for comparison with BGPS to check overall image quality, pointing, and flux calibration. The study of the Cygnus-X region by Motte et al. (2007) (hereafter M07) presents one of the largest fields in the Galactic plane that has been mapped with MABO which overlaps with the Bolocam survey fields.

The M07 Cygnus-X study used both the 37 element MAMBO and 117 channel MAMBO-2 instrument on the IRAM 30-meter diameter telescope on Pico Veleta in Spain. The FWHM beam size for the observations was 11''. The effective passband of the images presented by M07 is about 70 GHz centered at 240 GHz and thus includes the bright  $J = 2-1$  CO transition (see Figure 2).

The structure of the emission in the Cygnus-X region presented by Motte et al. (2007) appears nearly identical to the 1.1 mm Bolocam images of the same field despite the inclusion of the CO line, the slightly longer (by about 10%) longer effective wavelength, and different beam sizes. The peak positions also agree to within the errors of the BGPS, as discussed in this paper.

Direct comparison with the fluxes listed in M07 requires consideration of the factor of three difference in the size of the beams. For example, the brightest source in the Cyg-X region is DR 21. While M07 quote a peak flux density per beam of 4.2 Jy beam $^{-1}$  for the brightest feature in the DR 21 complex (their peak N46) and 17.9 Jy in a  $\sim 17''$  by  $23''$  box ( $0.19 \times 0.14$  pc at an assumed distance of 1.7 kpc; see M07 Table 1 in their Appendix). BGPS measures a peak flux of 17.5 Jy beam $^{-1}$  in an effective beam roughly 33'' in diameter, indicating that the relative calibration is similar on the brightest source in common to both surveys. However, DR 21 is an extended source. Fluxes are best compared using sources that appear compact as observed with the beam of the IRAM 30 meter telescope.

We have convolved the Motte et al. (2007) fits files<sup>2</sup> with a Gaussian kernel that generates an approximately 33'' beam, and compared the measured fluxes with those from the BGPS. Additionally, the data values in M07 are in units of Janskys per pixel, with each pixel subtending a 4'' by 4'' area on the sky. In contrast, the data values in BGPS are in units of Janskys per beam where the beam is 31'' in diameter. The conversion of units required multiplication of the convolved images by factor of 8.

The M07 images were convolved with IRAF task GAUSS using a 3.5 pixel convolution kernel to synthesize maps with an effective FWHM beam diameter of 33''; the BGPS maps have effective beam diameter 4'' larger than the CSO beam diameter of 31'' because of the smearing effects of optical distortion at the edges of the Bolocam array. This dis-

tortion has not been removed from the Version 1.0 images. The Bolocam flux calibration is based on the measurement of primary calibrators using the central pixels of the array which are not effected by distortion. The results are shown in Figure 6 and tabulated in Table 2. This figure and the table shows that BGPS and Motte et al. (2007) clumps have fluxes consistent within about 20% after convolution to a 33'' beam and scaling to Jy/beam.

The average M07 fluxes are larger than the BGPS fluxes by a factor of 1.23 despite the longer wavelength. Contamination by the bright CO  $J = 2-1$  line may account for a few percent of the excess detected flux by MAMBO. For a dust spectral index of  $-3.5$ , the MAMBO measurements should have detected a flux that is about 35% lower than what was seen by BGPS. If this is a typical spectral index for the sample of clumps, then the M07 flux calibration may be as much as 45% higher than the BGPS fluxes.

## 5. ASTROMETRY

### 5.1. Absolute Reference Sources and Pointing Model

We constructed an absolute reference system for the BGPS by observing bright quasars and blazars near the Galactic Plane [with small raster maps?]. The distribution of pointing sources over the sky is shown in Figure 7 and the list is given in Appendix C.

Pointing observations were performed approximately once every two hours over each night. The elevation offsets showed a deviation from zero which was empirically well-modeled by a quadratic function of elevation and a linear function of azimuth. No systematic deviation was observed for the azimuth offsets.

An RMS scatter of  $\sim 6''$  for the model over the entire observed range was achieved, with the scatter somewhat worse at the highest ZA. Further details of the pointing calculation are given in Appendix B.

### 5.2. Pixel Positions in the FOV

In addition to the model for the pointing center, it is necessary to empirically determine the actual projected pattern of the array on the sky, and measure the offset angle between the focal plane and the sky coordinate system. This is done by making observations which track all detectors across a bright source (e.g. a planet) and making maps from each bolometer individually.

In our first data release, the projected positions of the detectors on the sky are made using the nominal positions without correction for optical distortion. This results in a slightly blurred beam (33'' instead of 31''.2). Since a different subset of the array is used to map each portion of the scanned field, the effective beam size will vary slightly across the field, ranging from  $\sim 31''$  to  $\sim 33''$ , and it may be asymmetric. The effective beam size was measured from fully-sampled beam-mapping observations of plan-

<sup>2</sup> <ftp://cdsarc.u-strasbg.fr/pub/cats/J/A+A/476/1243/fits/>

ets, while the variation in beam size with sampling was measured from flux calibration observations of planets. The beam size at each position cannot be measured until distortion correction is performed in a later release.

Because this distortion is asymmetric, it can also result in a small pointing offset at the field edges where only bolometers with large offsets record data. However, this effect is strongly mitigated by the low number of hits at field edges - this data is generally flagged out. The residual offset is within the overall pointing model error, but caution should be used when measuring source locations at the field edges.

Because this distortion is asymmetric, it can also result in a small pointing offset at the field edges where only bolometers with large offsets record data. However, this effect is strongly mitigated by the low number of hits at field edges - this data is generally flagged out. The residual offset is within the overall pointing model error, but caution should be used when measuring source locations at the field edges.

A mean focus offset for the secondary was determined once per observing run. An elevation-dependent correction is applied via a CSO-determined look-up table between raster scans. We did not see any evidence that more frequent focus checks improve the quality of the PSF.

### 5.3. Relative Alignment and Mosaicing

Relative alignment between different observations of the same field was performed by finding the peak of the cross-correlation between images and a pointing master constructed from observations taken in the epoch with the best-constrained pointing model for that field (in most cases, this was from Epoch V, though in some cases Epoch VI was used). Each observation was initially mapped individually, then all observations in the pointing epoch were median-combined to create a reference field. Each observation was then cross-correlated with the reference image for that field. The cross-correlation peak was fit with a gaussian and the difference between the gaussian peak and the image center was used as the pixel offset. Finally, all observations of a field were merged into a single timestream with pointing offsets applied to create the field mosaic.

This method of alignment avoids the ambiguities inherent in using extracted sources to align fields, as the BGPS sources are rarely point-like. It further avoids the pointing smearing and loss of peak flux density which would result if the the maps of individual observations were coadded using the pointing model alone, where each individual observation would be coadded with the 6'' RMS uncertainty of the model. The relative alignment using the correlation maps is accurate to < 1'' [I think this should be the Gaussian width of the cross-correlation fit?] where there is adequate signal.

In low s/n fields, specifically  $l=65$  to 75, there was

not enough signal to acquire a pointing offset using cross-correlation. In these fields the relative pointing offset is larger and the beam is slightly larger.

### 5.4. Comparison to SCUBA Legacy Catalog Source Positions

All SCUBA 850 and 450  $\mu\text{m}$  data has been reprocessed in a uniform manner and made publicly available as the SCUBA Legacy Catalog (Di Francesco et al. 2008, hereafter SLC). These maps allow a cross-check of the accuracy of the BGPS pointing model. We have applied the same cross-correlation procedure used to obtain the relative alignment of BGPS observations to compare the BGPS images to the SLC. Concerns might arise in comparing the Bolocam to the SCUBA maps, such as the differing scan strategies (SCUBA maps were typically taken in jiggle-map mode, which tends to remove extended structure). The cross-correlation technique actually mitigates these effects, since it does not require the establishment of a single position for an object (which may differ due to the change in wavelength between the surveys or due to the observing strategy) but rather makes use of all the information available. The by-eye morphological comparison between SCUBA and BGPS sources is generally excellent with some exceptions, giving a high degree of confidence to the comparison and to the results obtained from the BGPS pointing model [include Di Francesco pointing accuracy]. An example is shown in Figure 9. We find that the RMS offset between BGPS and SLC positions within a  $3^\circ \times 1^\circ$  block defined by the BGPS is  $4.0 \pm 8.8''$ , consistent with the errors derived for the Bolocam pointing model. There were some BGPS fields that had larger offsets from SCUBA fields; these fields were excluded from the offset measurement above because of poor morphological match.

For the purposes of future comparison of both flux and pointing with other surveys, we present in Appendix D a selection of bright, compact, relatively isolated sources.

## 6. MAPPING ALGORITHM

The essential signal-processing problem to be solved by the mapping algorithm is the estimation and removal of a signal due to fluctuating atmospheric emission which is  $>\sim 100$ 's of times stronger than the typical sources in our maps. We implement an iterative procedure for estimating both the atmosphere fluctuations and the astrophysical signal without *a priori* knowledge of either.

We assume the raw timestream data  $d$  for each bolometer (indexed by  $i$ ) can be written as

$$d_i(t) = s_i(t) + a_i(t) + e_i(t) + \varepsilon_i(t) \quad (2)$$

where  $s$  is the astrophysical signal,  $a$  is atmospheric fluctuation noise,  $e$  are non-random signals due to the instrument itself, and  $\varepsilon$  is irreducible Gaussian noise due to photon shot and detector noise. The process of making a maximum likelihood map in the

presence of Gaussian noise is well-understood, and if the only contributions to the data were  $s$  and  $\varepsilon$ , then the minimum variance estimator of the true astrophysical map is given by

$$m = (A^T W A) A^T W d \quad (3)$$

where  $A$  encodes the pointing information and  $W$  is the inverse of the covariance matrix of the time domain noise  $\varepsilon$ ,

$$W = \langle \varepsilon_i \varepsilon_j \rangle^{-1} \quad (4)$$

In this case, the mapping from data to map is a linear operator,  $M = (A^T W A) A^T W$ . For compactness, Equation 3 will be written as  $M[d] = m$ . Note that the mapping operation is not invertible. However, given a map  $m$  and an observing matrix  $A$ , there exists a linear operation which makes predictions about the observed timestreams, namely  $d = Am$ ; this will be denoted  $T[m] = d$ . The goal is to produce a time series for each bolometer which as closely as possible approximates  $s + \varepsilon$  so that we may produce the best estimate of the astrophysical signal  $m = M[s + \varepsilon] = S + N$ .

We proceed iteratively, estimating  $a$  and  $e$  in the order of their relative strengths, beginning with the atmosphere. The first iteration step is then

$$\tilde{a}_i^{(n)}(t) = \sum_i d_i(t) - \tilde{s}_i^{(n)}(t) - \tilde{e}_i^{(n)}(t) \quad (5)$$

where  $\tilde{s}_i^{(0)}(t) = 0$ . Each bolometer's timestream is then fit to the mean atmosphere model

$$\tilde{a}_i^{(n)}(t) = \frac{d_i(t) \cdot a(t)}{d_i(t)^2} a(t) = r_i a(t) \quad (6)$$

This is illustrated in Figure 5. The  $r_i$  are then used as the relative gains of the detectors. Both the atmosphere and instrument models are subtracted from the raw time series

$$d_i(t) - \tilde{a}_i^{(n)}(t) - \tilde{e}_i^{(n)}(t) \approx s_i(t) + \varepsilon_i(t) \quad (7)$$

This is the best estimate of signal plus irreducible noise at iteration step  $n$ , and is made into a map

$$M[d_i(t) - \tilde{a}_i^{(n)}(t) - \tilde{e}_i^{(n)}(t)] = \tilde{m}^{(n)} \quad (8)$$

The current best map  $\tilde{m}^{(n)}$  is then deconvolved to provide a relatively low-noise, smooth map from which to generate a timestream

$$T[\mathcal{D}[\tilde{m}^{(n)}]] = \tilde{s}_i^{(n)}(t) \quad (9)$$

where  $\mathcal{D}$  represents the deconvolution operation. At this stage, the iterative process could begin again with Equation 5, though it is useful to produce a “residual map”

$$E = M[d_i(t) - \tilde{s}_i^{(n)}(t) - \tilde{a}_i^{(n)}(t) - \tilde{e}_i^{(n)}(t)] \quad (10)$$

This residual map serves as a visualization of the progress of the iterative method, since in a perfect process it would be map of  $\varepsilon$ .

### 6.1. Atmosphere Fluctuation Noise Model

By construction, the Bolocam beams as they pass through the dominant layer of atmospheric water vapor at  $\sim 1$  km altitude are still highly overlapped, and therefore sample a nearly identical region of atmosphere. The simplest model for the atmosphere fluctuations makes use of this fact by assuming that the largest correlated signals between detectors are due to the atmosphere correlations. However, the simple common mode subtraction of Equation 6 does not remove all of the correlated signal. To further remove the atmosphere (and other correlated instrument noise) without a detailed physical model, we use principal component analysis (PCA) as given in Laurent et al. (2005). While lacking the physical motivation of the polynomial subtraction used for the 2.1 mm Bolocam data by Sayers et al. (2009a), the 1.1 mm data seems to have a large number of correlated components that are not simply described by low-order polynomials in the focal plane. Figure 16 shows an example of the modes removed by the PCA model. In addition to the PCA model, after iteratively subtracting the astrophysical model, each scan has a polynomial fit in time removed to deal with the longest time scale modes.

### 6.2. Instrument Error Signals

Most of the instrument error signals have characteristic features which allow them to be identified, though not always removed. The error signals include the following:

1. Pickup from the 60 Hz AC power. This appears as narrow lines in the power spectral density (PSD) of the data. The second harmonic of 60 Hz is aliased via beating against the 130 Hz bolometer bias frequency into 10 Hz with sidebands split at  $\sim 1$  Hz. It is removed by replacing components at these frequencies in the Fourier transform with Gaussian noise matched to the local mean amplitude.
2. Spikes in voltage due to cosmic ray strikes on the bolometers (“glitches”).
3. Microphonic pickup due to vibrations of the receiver. The most noticeable microphonics occur at the end of each scan when the telescope is turning around and the field rotator is adjusting. This leads to broad spikes in the time series, whose long decay must be removed from the data, particularly during the beginnings of scans.

Fortunately, most of the AC powerline pick-up occurs at frequencies where there is no astrophysical signal, given the beam size and scan speed. Thus this error is dealt with by first notch filtering at the line frequencies and then low-pass filtering the data. Because of the low correlation with astrophysical

signal, this step is performed only once and is not iterated (c.f. Figure 1 of Sayers et al. (2009b)).

Both glitches and microphonic pickup from the scan turnarounds are degenerate with astrophysical signal and must be estimated as part of the iterative process. The turnaround microphonics are modeled as decaying exponentials at the beginnings and ends of scans and are also removed by the PCA cleaning.

### 6.3. Data Flagging

Due to the large volume of data generated by the survey, it was necessary to develop new tools to quickly visualize the data and ensure data quality. A common tool in radio astronomy is the so-called “waterfall” plot, which is an image with frequency on the x-axis, time on the y, and an intensity proportional to the interferometer visibility amplitude or phase. We have used a variant on this to visualize the Bolocam data by displaying bolometer number (related to the bolometer position in the focal plane) on the x-axis and time on the y, with the intensity given by the bolometer’s response (in Jy) at that time. An example of this is shown in Figure 13a. Anomalies such as the glitch shown can be detected and manually and interactively flagged out.

An automated flagger was also created that flags out outlier data on a per-map-pixel basis. In order to make a robust measurement of the variance of the fluxes assigned to each pixel, we used the median average deviation (MAD) over the data in the pixel and rejected high and low outliers at the 3-sigma level. Pixels with too little data to compute a deviation, i.e. those with  $< 3$  data points, were also flagged out - these scan-edge pixels are the dominant contribution to the total number of flagged data points.

### 6.4. Creation of the Astrophysical Model

The timestream data is made into a spatial map using the pointing data corresponding to each time point for each bolometer. The data is weighted by inverse variance across a single scan and then drizzled into a map with  $7.2''$  pixels using a nearest-neighbor algorithm. The nearest-neighbor matching allows the map to be returned to a timestream in the same manner, but with the S/N improved by averaging over all hits on a given pixel. It has the disadvantage that it accentuates the unevenness of the cross-scan sampling, since each timestream point’s value is assigned to an area much smaller than the beam. In principle this can be addressed by various gridding algorithms, and may be a part of future reductions of the BGPS data.

The resulting map is then subjected to a maximum-entropy clean algorithm (Hollis et al. 1992) using a specified kernel to produce a deconvolved image which is mapped back into the timestream to be subtracted (Equation 9). This has several advantages over using the original map directly, including rejecting artifacts smaller than the kernel and decreasing the noise of the result-

ing timestream. It is also better than a “threshold” method, which tends to produce discontinuities and include noise outliers.

In some fields, flux from some sources spread out over the course of the iterative process using certain kernel sizes. The cause of this artifact is not yet well-understood, but using a different kernel size was an effective workaround and did little to change the properties of the final map. The standard kernel size was  $14.4''$ ; a  $21.6''$  kernel was used when artifacts were encountered. Simulations indicate that this change in kernel has a negligible effect on the flux of the source; see Figure 19.

## 7. NOISE AND SYSTEMATIC EFFECTS

The residual maps  $E$  (Equation 10) form the basis for the noise estimation and also provide a way of estimating the systematic error resulting from imperfect subtraction of bright sources. These maps are produced for each region from the data residuals after removing the astrophysical signal model and the PCA atmosphere model. An example of an error map is shown in Figure 20. In an ideal case, the residual map  $E$  represents a map of a realization of the underlying irreducible noise  $\varepsilon$ . However, the imperfect estimation of the signal results in positive “ghosts” of bright sources. We have found that smoothed versions of the residual maps provide the best means of determining the pixel-to-pixel error that account for the local variations in the noise, including those due to such artifacts. Our pixel noise estimate assumes the noise is uncorrelated between adjacent pixels, but of course adjacent spatial pixels are correlated due to residual atmospheric noise correlated in time. We have ignored this effect in our analysis under the assumption that the remaining correlations after subtracting the PCA model are small.

Because observing conditions varied widely during the survey, the RMS noise levels obtained in the various fields of the BGPS also varies. However, the noise within a given  $1^\circ \times 1^\circ$  field is fairly uniform in the absence of very bright sources. We show the variation of the depth as a function of Galactic longitude in Figure 18.

## 8. EFFECTS OF THE DATA REDUCTION PROCEDURES ON PHOTOMETRY

To do accurate and meaningful photometry on the Bolocam maps requires a good estimate of the noise (Section 7) but also an understanding of the spatial filtering imposed by the observing strategy and the cleaning and mapping of the data. The additional complexities of defining “sources” in complicated regions are discussed in Rosolowsky et al. (2009). Here we restrict our discussion to the limitations on performing photometry imposed by the data reduction.

The fundamental feature of the data is that there is a degeneracy between large spatial scale astrophysical emission and the atmosphere and other signals with long spatial or temporal variations. Con-

sequently, there are limits to ability of the algorithm to separate the signal  $s$  from the atmosphere  $a$  and instrument terms  $e$  in Equation 7. Inevitably, some of the signal which should be present in  $s$  is mixed into these terms and is thus not present in the final map  $m$ . Because  $s$  is generated from a deconvolution algorithm, it has non-zero mean by construction, but importantly, it does *not* contain an unbiased estimate of the astrophysical signal on all spatial scales: large spatial scales are preferentially missing.

To assess the effect of the mapping algorithm on the flux recovered as a function of angular scale, we performed a series of simulations. Gaussian sources with a range of peak flux densities and sizes were inserted on top of a background consisting of real BGPS data with the astrophysical source model removed. The recovered fluxes were measured in ellipses that included single well-separated sources. Figure 19a shows the fraction of flux recovered in the map as a function of source size for a range of different PCA components subtracted in the cleaning.

The final reduction used 13 PCA components because this produced a reasonable compromise between attenuating extended structure and cleaning the atmospheric contribution. Note that this is a substantially more aggressive cleaning than that used in Enoch et al. (2006) largely because our mean integration time per pixel was  $\sim$ seconds, whereas theirs was  $\sim$ minutes.

Figure 19b shows the fraction of flux recovered in the maps as a function of the deconvolution kernel used to create the astrophysical model maps. The differences at large source sizes are not well-understood (these size scales may be dominated by atmosphere), but at the smallest source size, it is evident that a deconvolution kernel smaller than the source size does not reliably recover the source flux. Therefore we chose a deconvolution kernel smaller than the beam but larger than the pixel size used. Figure 17 demonstrates the effects of using both too large and too small a kernel.

## 9. FINAL MAPS AND DATA RELEASE

The final maps are produced by coadding all observations of a single square degree centered on a particular Galactic coordinate  $(l_0, b_0)$ . The maps are made in Galactic coordinates using a plate carré (FITS header CAR) projection. (This is the same projection used by the *Spitzer*-GLIMPSE and BUFCRAO GRS surveys.) As these maps are near the coordinate system equator, the difference between truly equiareal pixels and the pixels used is at most even at  $5^\circ$ out of the plane (as for IC1396) is 0.4%. The pixel size is  $7.2''$ , chosen to be much smaller than the Bolocam beam. The maps are written to standard FITS files. An example of the FITS header for the BGPS images is given in Appendix E.

Five image types will be released, each covering the same regions. The maps are standard astrophys-

ical maps subject to the caveats previously mentioned, the most important being the spatial filtering function (section 7).

All processed maps are available through IPAC<sup>3</sup>. IPAC provides a cutout service for the images as well as a searchable version of the catalog provided in Rosolowsky et al. (2009). The full release includes:

1. Calibrated maps for all regions observed (MAP).
2. The deconvolved MAP (MODEL). The model maps are deconvolved using the maximum-entropy method with kernels specified in the header (either  $14.4''$  or  $21.6''$ ). After deconvolution, the maps are smoothed to the beam size of  $33''$ .
3. Maps of integration time per pixel (NHITSMAP). The nhitsmap shows how many recorded data points from the timestream have been assigned to each pixel; it is proportional to the dwell time per pixel (each ‘hit’ is .1s).
4. Maps of residual noise per pixel (RESIDUAL). The residual map is the map of the model timestream subtracted from the data timestream; it is close to but not identical to the map minus the model.
5. Maps of inverse variance per pixel (WEIGHTMAP). The weightmap shows the inverse-variance weighting of each pixel.
6. Maps of the mask obtained for various regions from the cataloging algorithm (MASKMAP) (Rosolowsky et al. 2009)

Examples of each (except the nhitsmap) are given in figure 20.

## 10. DISCUSSION

The BGPS is the first millimeter survey of a substantial fraction of the Galactic Plane, providing an unbiased look at the high-density gas most intimately associated with the earliest phases of star formation. Maps of the entire BGPS are presented in Figure 21.

Inspection of Figure 21 shows excellent correspondence with SCUBA maps of small sub-fields throughout the plane (Di Francesco et al. 2008). BGPS contours overlaid on the GLIMPSE survey (Benjamin et al. 2003) show excellent correlation with  $8\mu\text{m}$  infrared dark clouds (IRDCs). However, many features in the BGPS maps do not appear in the Spitzer observations, which suggests that the 1.1 mm emission traces dense clumps without a background to absorb; see Figure 22.

<sup>3</sup> <http://irsa.ipac.caltech.edu/Missions/bolocam.html>

Filamentary structures with aspect ratios  $\geq 10$  are present throughout the galactic plane. The most crowded fields consist of frothy and clumpy structure. There are 5000-10000 distinct sources, the majority of which are at least moderately resolved (Rosolowsky et al. 2009). We suspect that higher resolution observations will resolve BGPS clumps into clusters of protostellar objects, as has been seen in Serpens (Enoch et al. 2008; Testi & Sargent 1998), OMC 1 (Beuther et al. 2004; Johnstone & Bally 1999), and S255N (Cyganowski et al. 2007) where bolometer observations at low resolution have been complemented by interferometer observations at high resolution.

There are clear maxima in the emission filling factor in the Galactic Center and in the region from  $l = 23$  to  $l = 31$ , the line of sight through the densest part of the molecular ring. Additional areas of high source density are seen at  $l = 10$  and  $l = 13$ . The filling factor of 1.1 mm continuum emission at the 100 mJy level is  $\sim 20\%$  per square degree from  $l = -10$  to  $l = 20$  and  $\sim 10\%$  from  $l = 20$  to  $l = 50$  (compare to figure 18). In the range  $l = 50$  to  $l = 75$ , the filling factor is below 1% and very few sources have been detected. This result is in contrast to CO filling factors  $\sim 1$  in the inner galactic plane (Dame et al. 2001; Jackson et al. 2006), confirming that 1.1 mm continuum emission traces denser material than CO. The small filling factor of the 1.1 mm emission compared to CO emission shows that the continuum is directly associated with star forming material, whereas the CO also traces less dense material not directly associated with star formation.

In some cases, distance to BGPS clumps can be determined by matching Galactic Ring Survey  $^{13}\text{CO}$  and 1.1 mm continuum morphology (Simon et al. 2006; Jackson et al. 2006). However, in other cases the association between the CO and 1.1 mm data is not clear, either because of confusion or because the BGPS sources are too compact to identify in  $^{13}\text{CO}$  morphology. Heterodyne follow-up observations using dense gas tracers ( $\text{NH}_3$ ,  $\text{N}_2\text{H}^+$ ,  $\text{HCO}^+$ , and CS) are being conducted to provide radial velocity, density, chemistry, and temperature measurements (Schlingman et al. 2009; Battersby et al. 2009; Nordhaus et al. 2009).

The depth can be converted into an estimate of mass via standard estimates, i.e., under the assumption of a temperature, opacity, and distance. Using

dust opacity from Ossenkopf & Henning (1994) and assuming a gas-to-dust mass ratio 100, the mass sensitivity can be written as

$$M_{\text{gas}} \approx 0.22 \left( e^{13.1/T_d} - 1 \right) \left( \frac{S_\nu}{15 \text{ mJy}} \right) D_{\text{kpc}}^2 M_\odot \quad (11)$$

where  $D_{\text{kpc}}$  is the distance to the source in kpc. (At  $S_\nu = 15$  mJy this corresponds to an RMS extinction sensitivity of  $A_V \sim 1$  mag, with the same  $T_d$  dependence). For Bolocam,  $h\nu/k \approx 13$  K, so for  $T_d > 10\text{K}$  the dependence is approximately linear. At the coldest temperatures expected, the mass changes a factor of 2.9 between 20 and 10 K. The distance to the clump is more important in most situations.

BGPS clumps are associated with the densest portions of giant molecular clouds (GMCs) traced by CO surveys (e.g., Dame et al. 2001; Jackson et al. 2006). The brightest clumps visible in our maps, e.g. Sgr B2, G34.3+0.15, W 51, W 43, W 49, and M 17, correspond to well known star forming regions. These associations suggest that other bright sources of millimeter emission will prove to be massive star or cluster forming regions.

We anticipate that the public release of the BGPS data will serve as an important first look to help guide HIGAL, JPS, ...

---

*Facilities:* CSO (Bolocam)

We would like to acknowledge the staff and day crew of the CSO for their assistance. The BGPS project is supported by the National Science Foundation through NSF grant AST-0708403. J.A. was supported by a Jansky Fellowship from the National Radio Astronomy Observatory (NRAO). The first observing runs for BGPS were supported by travel funds provided by NRAO. Support for the development of Bolocam was provided by NSF grants AST-9980846 and AST-0206158. Team support was provided in part by NSF grant AST-0607793 to the University of Texas at Austin.

We recognize and acknowledge the cultural role and reverence that the summit of Mauna Kea has within the Hawaiian community. We are fortunate to conduct observations from this mountain.

## APPENDIX

### CALCULATION OF COLOR CORRECTIONS

If an experiment has finite bandwidth ( $t(\nu) \neq \delta(\nu - \nu_c)$ ), to report a source surface brightness at a single frequency, one must assume a source spectrum. The power detected from that source is assumed to be

$$P_{\text{in}} = \eta A\Omega \int I_0(\nu)t(\nu)d\nu \quad (\text{A1})$$

(Here  $\eta$  and  $A\Omega$  are the optical efficiency and throughput of the instrument,  $I_0(\nu)$  is the nominal (assumed) surface brightness of the source, and  $t(\nu)$  is the bandpass transmission normalized to 1.0 at its peak.) The

effective band center  $\nu_c$  is usually chosen such that

$$I_0(\nu_c) \simeq \frac{\int I_0(\nu)t(\nu)d\nu}{\int t(\nu)d\nu} \quad (\text{A2})$$

The band centers for Bolocam are calculated assuming a Rayleigh-Jeans (RJ) source spectrum

$$\begin{aligned} I_0(\nu_c) &= I_{RJ}(\nu_c) \\ &= \tau 2kT \frac{\nu_c^2}{c^2}, \end{aligned} \quad (\text{A3})$$

where  $\tau$  is the optical depth of the source and  $k$  is Boltzmann's constant. Since the detected power is assumed to be

$$P_{in} = \eta A\Omega \int \tau 2kT \frac{\nu^2}{c^2} t(\nu)d\nu, \quad (\text{A4})$$

we can write

$$I_0(\nu_c) = \frac{P_{in}}{\eta A\Omega \int \nu^2 t(\nu)d\nu} \nu_c^2 \quad (\text{A5})$$

Now if we assume a different source spectrum, for example a greybody with power-law emissivity, the assumed input power is

$$\begin{aligned} P_{in} &= \eta A\Omega \int I_{GB}(\nu)t(\nu)d\nu \\ &= \eta A\Omega \int \tau(\nu_0)(\nu/\nu_0)^\alpha B_\nu(T)t(\nu)d\nu \end{aligned} \quad (\text{A6})$$

and the source spectrum inferred from the detected power is

$$\begin{aligned} I_{GB}(\nu_c) &= \tau(\nu_0)(\nu_c/\nu_0)^\alpha B_{\nu_c}(T) \\ &= \frac{P_{in}}{\eta A\Omega \int \nu^\alpha B_\nu(T)t(\nu)d\nu} \nu_c^\alpha B_{\nu_c}(T) \\ &= \frac{\int \nu^2 t(\nu)d\nu}{\int \nu^\alpha B_\nu(T)t(\nu)d\nu} \nu_c^{\alpha-2} B_{\nu_c}(T) I_{RJ}(\nu_c) \\ &\equiv \frac{I_{RJ}(\nu_c)}{K}. \end{aligned} \quad (\text{A7})$$

This defines the color correction  $K$  to apply to the reported Bolocam flux from a source if the source is assumed to have a greybody spectrum with power-law emissivity.

We note that for an arbitrary experiment with bandpass  $t(\nu)$  that reports its surface brightness measurements assuming a spectrum  $I_0(\nu)$ , the surface brightness assuming a different source spectrum  $I_1(\nu)$  is given by

$$\begin{aligned} I_1(\nu_c) &= I_0(\nu_c)/K \\ &= I_0(\nu_c) \frac{I_1(\nu_c)}{\int I_1(\nu)t(\nu)d\nu} \left[ \frac{I_0(\nu_c)}{\int I_0(\nu)t(\nu)d\nu} \right]^{-1} \end{aligned} \quad (\text{A8})$$

#### POINTING CALCULATION

To calculate the position at which to point the telescope, the CSO antenna computer computes an alt/az ( $E, A$ ) derived from the RA/Dec J2000 (heliocentric) catalog position. It performs the following calculation:

1. Precess catalog coordinates to current epoch. The CSO by default stores catalog positions in B1950.
2. Add aberration and nutation corrections. This is the “requested apparent” RA and Dec reported by the antenna computer.
3. The equatorial coordinates are transformed to horizon coordinates using the current local apparent sidereal time.
4. An 11-term model (“C-terms”) based on the optical pointing of the telescope is then applied to  $A$  and  $E$  along with  $t$ -terms (?), the tilt of the alidade, and a refraction correction to obtain the necessary mechanical pointing of the telescope to acquire the source.

TABLE 1  
COMPARISON OF BAND CENTERS AND FLUX  
RATIOS FOR BOLOCAM AND MAMBO.

$\alpha$	MAMBO $\nu_c$ [GHz]	Bolocam $\nu_c$ [GHz]	$S_{\text{BOLOCAM}} / S_{\text{MAMBO}}$
1.0	254.8	267.8	1.051
1.5	256.4	268.6	1.072
2.0	258.0	269.4	1.090
2.5	259.5	270.0	1.104
3.0	261.1	270.7	1.115
3.5	262.5	271.4	1.124
4.0	264.0	272.2	1.130
4.5	265.4	272.9	1.134
5.0	266.8	273.8	1.137

5. The telescope then attempts to follow this track; the difference between the requested  $A, Z$  and the actual, measured angles of the encoders (a result of servo errors) are also reported.

The CSO antenna computer reports this pointing information, including geocentric RA/Dec, at a rate of 100 Hz. This time series, along with the field rotator encoder information from Bolocam is merged with the bolometer time series and aligned.

To calculate the pointing used in the map from the telescope inputs, the Bolocam software does the following:

1. Start with the reported  $\alpha', \delta'$  from the CSO. Remove aberration and nutation corrections. Precess from current epoch to J2000. This gives  $\alpha, \delta$ .
2. Apply the  $\Delta A, \Delta E$  terms to  $\alpha, \delta$  to account for the difference between commanded and actual positions of the telescope.

TABLE OF ABSOLUTE POINTING SOURCES

The absolute reference frame for the BGPS pointing model was chosen from a selection of bright quasars near the Galactic Plane. Table 2 gives the pointing sources used for this purpose.

TABLE 2  
ABSOLUTE POINTING CALIBRATORS

Number	Alias	RA(J2000)	Dec(J2000)	l	b	Flux (Jy)
1	1622-253	16 25 46.9	-25 27 38.3	352.14	16.32	0.18
2	16293-2422	16 32 22.9	-24 28 35.6	353.94	15.84	8.40
3	1657-261	17 00 53.2	-26 10 51.7	356.70	9.75	0.07
4	NGC6334I	17 20 53.4	-35 47 1.7	351.42	0.64	2.50
5	NRAO530	17 33 02.7	-13 04 49.5	12.03	10.81	2.70
6	1741-038	17 43 58.8	-3 50 4.6	21.59	13.13	1.44
7	1749+096	17 51 32.8	9 39 0.7	34.92	17.65	2.70
8	G5.89	18 00 30.4	-24 04 0.5	5.89	-0.39	3.57
9	M8E	18 04 53.0	-24 26 39.4	6.05	-1.45	3.92
10	G10.62	18 10 28.7	-19 55 49.8	10.62	-0.38	17.20
11	1830-211	18 33 39.9	-21 03 40.0	12.17	-5.71	1.70
12	G34.3	18 53 18.6	1 14 58.3	34.26	0.15	31.30
13	1908-202	19 11 09.6	-20 06 55.0	16.87	-13.22	1.00
14	G45.1	19 13 22.1	10 50 53.4	45.07	0.13	3.70
15	OV236	19 24 51.0	-29 14 29.8	9.34	-19.61	8.60
16	1923+210	19 25 59.6	21 06 26.1	55.56	2.26	0.32
17	1954+513	19 55 42.7	51 31 48.6	85.30	11.76	0.60
18	CYGA	19 59 28.5	40 44 1.7	76.19	5.75	0.25
19	K3-50	20 01 45.7	33 32 43.5	70.29	1.60	8.45
20	2005+403	20 07 44.9	40 29 48.6	76.82	4.30	0.40
21	ON1	20 10 09.1	31 31 37.7	69.54	-0.98	2.90
22	2013+37	20 15 28.7	37 10 59.6	74.87	1.22	1.40
23	2021+317	20 23 19.0	31 53 2.4	71.40	-3.10	0.54
24	2023+336	20 25 10.8	33 43 0.3	73.13	-2.37	0.92
25	GL2591	20 29 24.7	40 11 18.9	78.89	0.71	2.07
26	MWC 349	20 32 45.5	40 39 36.7	79.64	0.47	1.67
27	W75N	20 38 36.4	42 37 34.5	81.87	0.78	4.46
28	3C418	20 38 37.0	51 19 12.7	88.81	6.04	0.62
29	CRL 2688	21 02 18.8	36 41 37.7	80.17	-6.50	1.90
30	NGC7027	21 07 01.6	42 14 10.2	84.93	-3.50	9.27
31	2201+315	22 03 15.0	31 45 38.4	85.96	-18.78	0.35

TABLE 3  
IN-PLANE MILLIMETER SOURCES

Number	Alias	RA(J2000)	Dec(J2000)	l	b	Flux (mJy)
l351pps		17 23 50.2	-36 38 58.8	351.04	-0.34	-999.0
l354pps		18 00 50.0	-23 20 33.0	6.55	-0.10	-999.0
l357pps		17 40 57.3	-31 10 48.0	357.56	-0.32	-999.0
l000pps		17 46 37.1	-29 10 21.5	359.91	-0.31	-999.0
l000pps2		17 47 10.3	-28 46 11.8	0.32	-0.20	-999.0
l002pps		17 50 36.3	-27 06 2.8	2.14	0.01	-999.0
l006pps		17 57 34.4	-23 58 12.0	5.64	0.24	989.0
l009pps		18 06 14.2	-20 31 58.0	9.61	0.19	1187.0
l009pps2		18 06 15.5	-20 32 8.0	9.61	0.19	1189.0
l012pps		18 10 50.5	-17 55 54.0	12.42	0.51	1205.0
l015pps		18 14 35.3	-16 45 45.0	13.87	0.28	1085.0
l015pps2		18 21 08.5	-14 31 48.0	16.58	-0.05	748.0
l018pps		18 25 42.0	-13 10 13.0	18.30	-0.39	1544.0
l020pps		18 28 09.9	-11 28 47.0	20.08	-0.13	1650.0
l021pps		18 30 34.0	-9 34 54.0	22.04	0.22	993.0
l023pps		18 34 54.6	-8 49 18.0	23.20	-0.38	1681.0
l024pps		18 36 05.1	-7 31 21.0	24.49	-0.04	1851.0
l025pps		18 36 16.7	-6 43 8.7	25.23	0.29	-999.0
l026pps		18 37 18.4	-6 38 38.4	25.41	0.10	-999.0
l026pps2		18 39 04.9	-6 24 23.6	25.82	-0.18	-999.0
l027pps		18 41 51.1	-5 01 48.0	27.36	-0.17	3478.0
l028pps		18 44 19.0	-4 40 52.0	27.95	-0.55	-999.0
l028pps2		18 42 51.8	-4 00 1.9	28.39	0.08	-999.0
l029pps		18 42 15.6	-3 34 44.5	28.70	0.41	-999.0
l028pps2		18 42 50.8	-3 59 46.1	28.40	0.09	-999.0
l033pps		18 52 25.1	0 14 53.0	33.26	-0.11	-999.0
l035pps		18 53 39.1	1 50 32.0	34.82	0.35	756.0
l037pps		18 59 10.0	4 12 10.0	37.55	0.20	1045.0
l038pps		19 01 53.2	4 12 51.0	37.87	-0.40	1487.0
l040pps		19 05 40.9	6 26 5.0	40.28	-0.22	1700.0
l042pps		19 10 33.5	9 08 7.0	43.23	-0.05	1247.0
l044pps		19 11 54.4	9 35 53.0	43.80	-0.13	1829.0
l044pps2		19 13 28.4	10 53 41.0	45.12	0.13	1999.0
l048pps		19 23 10.8	14 26 31.0	49.37	-0.30	1903.0
l050pps		19 23 11.1	14 26 34.0	49.37	-0.30	2088.0
l079pps		20 29 25.3	40 11 28.0	78.89	0.71	1390.0
l079pps		20 29 25.2	40 11 30.0	78.89	0.71	2014.0
l079pps2		20 31 13.3	40 03 33.0	78.99	0.35	790.0
l080pps		20 34 42.8	39 44 45.0	79.13	-0.37	1104.0
l080pps2		20 40 05.3	41 31 48.0	81.17	-0.11	961.0
l080pps		20 30 28.7	41 16 6.0	79.88	1.18	1024.0
l082pps		20 40 26.8	41 56 54.0	81.54	0.10	805.0
l110.5npps		23 05 10.7	60 14 50.6	110.11	0.05	-999.0
l111pps		23 15 31.5	61 07 39.7	111.62	0.38	-999.0
l134p1		02 29 02.8	61 33 31.2	134.28	0.86	-999.0
l134p1-2		02 27 06.9	61 52 20.8	133.95	1.07	-999.0
l134p1-3		02 27 02.4	61 52 32.9	133.94	1.07	-999.0
l135p1		02 34 45.1	61 46 23.0	134.83	1.31	-999.0
l136p15		02 50 08.4	61 59 56.7	136.38	2.27	-999.0
l137p15		02 29 03.2	60 43 26.9	134.59	0.08	-999.0
IC1396		21 40 11.5	58 16 11.7	99.93	4.21	-999.0
IC1396-2		21 36 36.8	57 30 50.0	99.07	3.97	-999.0
IC1396-3		21 35 38.4	57 26 40.5	98.93	4.00	-999.0
l189pps		06 08 50.1	21 38 19.0	188.94	0.87	-999.0
l189pps-2		06 08 49.7	21 38 5.7	188.95	0.87	-999.0
l192pps		06 12 51.5	18 00 39.3	192.58	-0.05	-999.0
l192pps-2		06 12 51.5	17 59 36.3	192.59	-0.05	-999.0
l192pps-3		06 12 50.1	18 00 35.8	192.58	-0.05	-999.0
l192pps-4		06 12 50.3	17 59 28.8	192.59	-0.06	-999.0
l192pps-5		06 07 43.9	20 39 29.6	189.67	0.17	-999.0

TABLE OF REFERENCE SOURCES  
FITS HEADER INFORMATION

```

SIMPLE = T / Written by IDL: Sun Jan 18 01:21:05 2009
BITPIX = -32 / Number of bits per data pixel
NAXIS = 2 / Number of data axes

```

```
NAXIS1 = 3134 /
NAXIS2 = 883 /
DATE = '2009-01-18' / Creation UTC (CCCC-MM-DD) date of FITS header
LONPOLE2= 180.00000 /lonpole
LATPOLE2= 0.0000000 /latpole
PPBEAM = 21.276915 /pixels per beam
CALIB_0 = -0.00333379 / 0th coefficient for flux cal
CALIB_1 = -2.92617 / 1st coefficient for flux cal
CALIB_2 = 6.97269 / 2nd coefficient for flux cal
ITERNUM = 0 /Iteration number
N_PCA = 0 /number of PCA components subtracted
COMMENT FITS (Flexible Image Transport System) format is defined in 'Astronomy
COMMENT and Astrophysics', volume 376, page 359; bibcode 2001A&A...376..359H
CTYPE1 = 'GLON-CAR' / Coordinate Type
CTYPE2 = 'GLAT-CAR' / Coordinate Type
EQUINOX = 2000.00 / Equinox of Ref. Coord.
CD1_1 = -0.00199999986216 / Degrees / Pixel
CD2_1 = 0.000000000000 / Degrees / Pixel
CD1_2 = -0.000000000000 / Degrees / Pixel
CD2_2 = 0.00199999986216 / Degrees / Pixel
CRPIX1 = 1270.52 / Reference Pixel in X
CRPIX2 = 366.367 / Reference Pixel in Y
CRVAL1 = 191.092003456 / Galactic longitude of reference pixel
CRVAL2 = 0.0993870183708 / Galactic latitude of reference pixel
PV2_1 = 0.000000000000 /Projection parameter 1
HISTORY PUTAST: Jan 18 01:10:42 2009 World Coordinate System parameters written
END
```

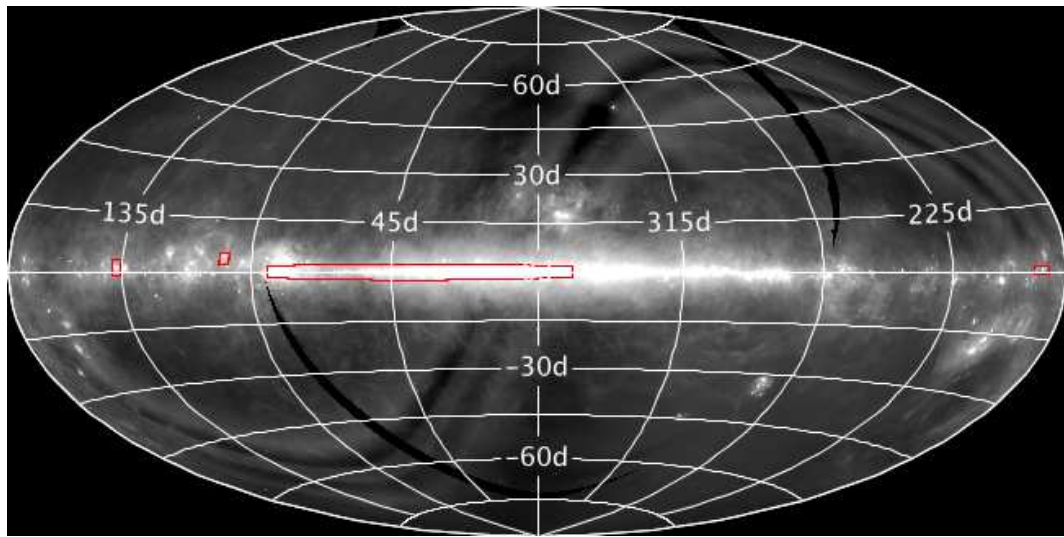


FIG. 1.— The coverage of the BGPS. The background greyscale is IRAS 100  $\mu\text{m}$ .

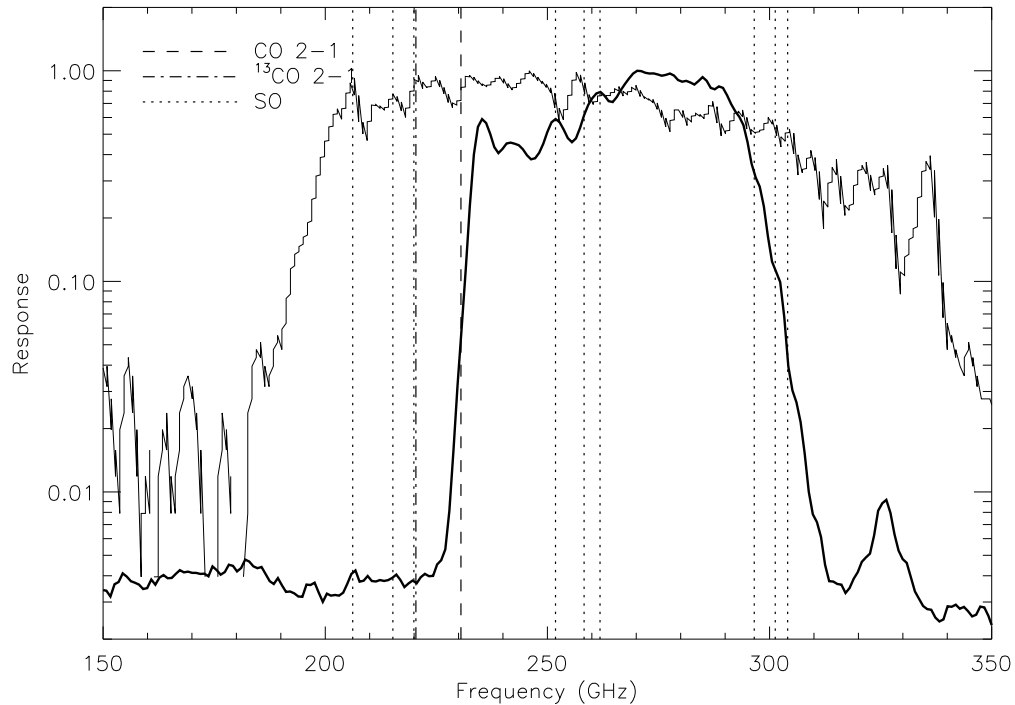


FIG. 2.— The Bolocam 1.1 mm bandpass. Bright molecular emission lines are shown at their rest frequencies. Note that the Bolocam passband rejects > 90% of the  $^{12}\text{CO}$  flux, leaving our continuum measurements largely uncontaminated.  $\text{SO}_2$  and  $\text{CH}_3\text{OH}$  lines are likely strong contributors to line flux in the passband. Nummelin et al. (1998) found that 22% of the flux density in one pointing towards Sgr B2 was from lines, and Yoshida & Phillips (2005) reported > 40% in Orion A from line emission over the 260-328 GHz band. Other lines lying in the Bolocam passband include CS(5  $\rightarrow$  4) and (6  $\rightarrow$  5) (245 and 293 GHz), HCN(3  $\rightarrow$  2) (265 GHz) and  $\text{HCO}^+(3 \rightarrow 2)$  (267 GHz).

TABLE 4  
OBSERVING EPOCHS FOR THE BGPS

Number	Begin (UT)	End (UT)	Nights	$\tau_{225}$
I	2005 Jul 03	2005 Jul 13	5	0.1
II	2005 Sep 04	2005 Sep 12	5	0.1
III	2006 Jul 01	2006 Jul 13	5	0.1
IV	2006 Sep 01	2006 Sep 09	5	0.1
V	2007 Jul 01	2007 Jul 13	5	0.1
VI	2007 Sep 01	2007 Sep 09	5	0.1

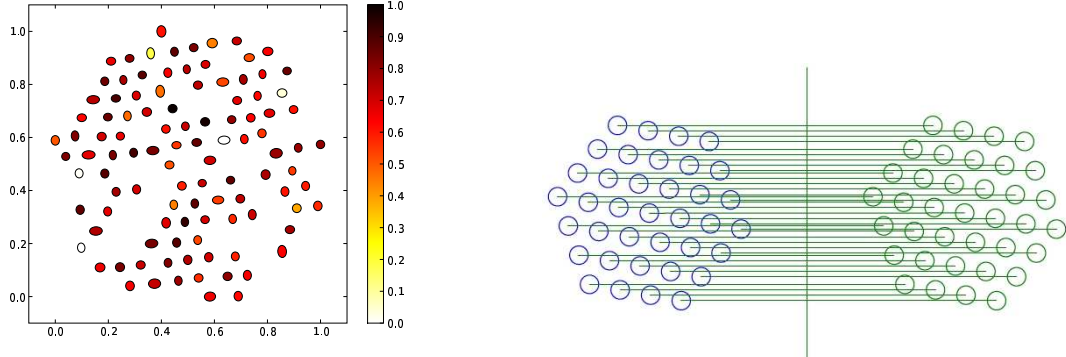


FIG. 3.— Left: the position, ellipticity and relative response of the detectors in the Bolocam focal plane as mapped to the sky. Right: The effect of field rotation on the coverage obtained via Bolocam raster scans. The array is held fixed during a scan, but is rotated relative to the scan direction such that the sampling is most uniform by attaining the best sampling in the cross-scan direction.

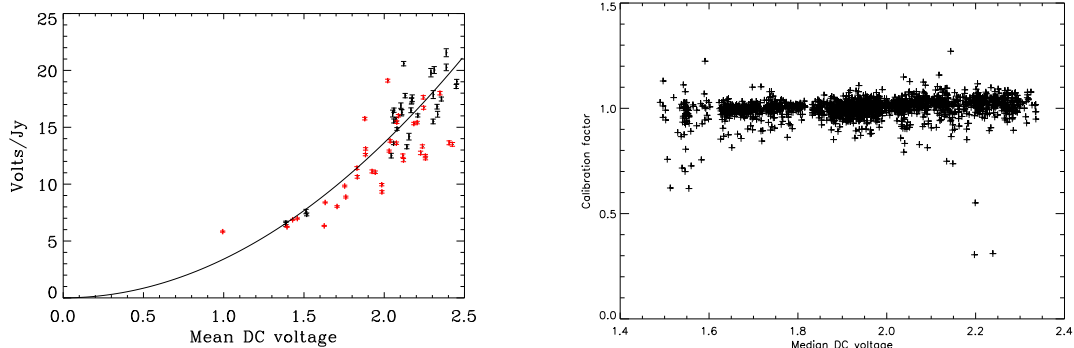


FIG. 4.— Left: Average calibration curve [V/Jy] versus the mean detector voltage, a proxy for atmospheric loading. Red points are observations of Mars and black of Uranus. The black line is a 2nd-order fit with 0,0 forced (no response if no measurable potential difference). Right: Scaling of the relative response to the atmosphere for a single detector compared to the array median. Outliers are from noisy scans that are strongly downweighted.

TABLE 5  
FLUX DENSITY ERROR BUDGET

Source	Contribution
Pointing error uncertainty	2%
Calibration curve (Eq. 1) uncertainty	< 5%
PCA flux reduction uncertainty	4%
Absolute Mars flux uncertainty	5%
Beam size uncertainty (surface brightness)	X%
Total	7% (random) + 5% (systematic)

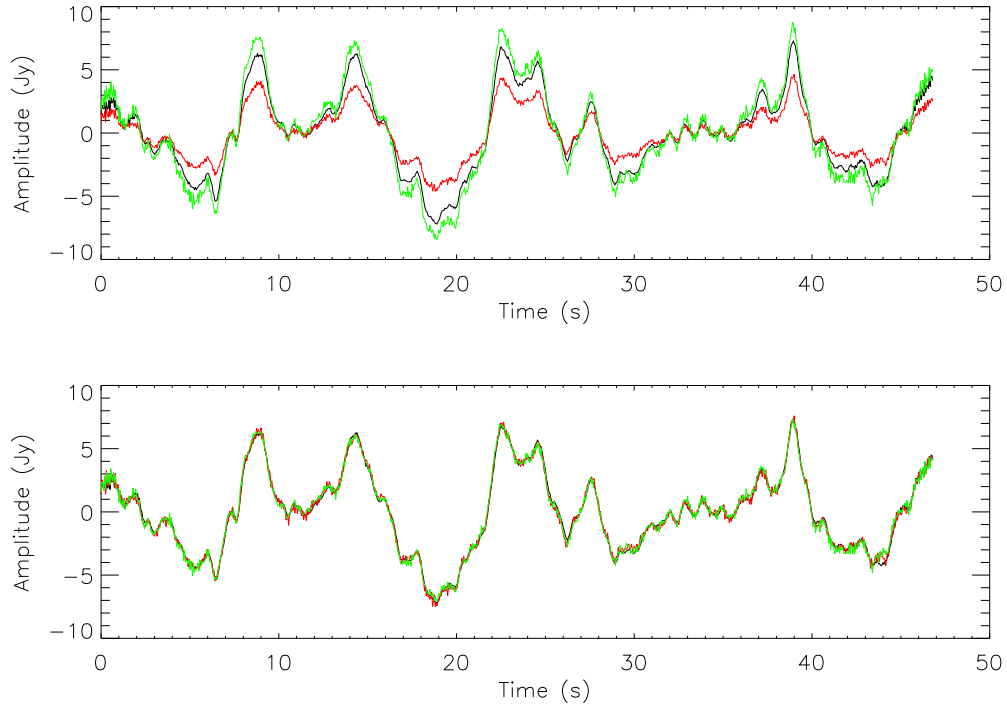


FIG. 5.— An illustration of the relative sensitivity calibration using the atmosphere as a calibrator. Black is the median over all bolometers (the 1st-order atmosphere model), red and green are individual bolometers. a. before and b. after applying the relative calibration. Note the improved agreement.

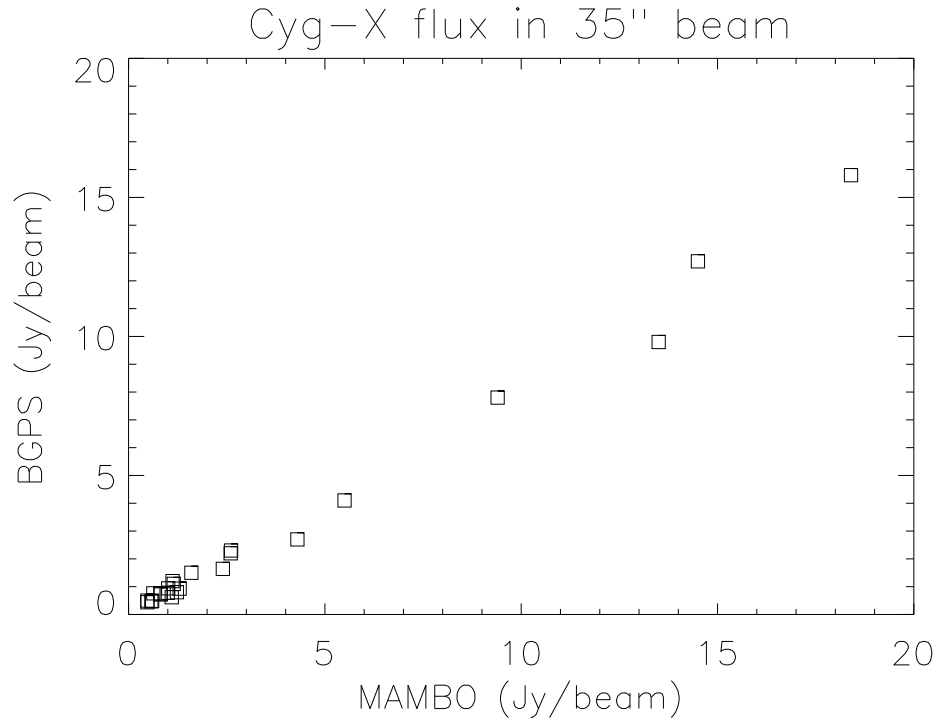


FIG. 6.— A comparison of the fluxes extracted in the same aperture from the Motte et al. (2007) MAMBO map and the Bolocam map of this paper.

TABLE 6

COMPARISON OF MOTTE ET AL. (2007) IRAM AND BGPS MEASUREMENTS IN THE CYGNUS X REGION. THE IRAM DATA HAS BEEN CONVOLVED TO THE BGPS BEAM AND SCALED SO THE UNITS ARE IN JY/BEAM.

M07 Source Number	M07 Table 1 integrated flux	M07 scaled Jy beam <sup>-1</sup>	BGPS Jy beam <sup>-1</sup>	Ratio	Comments
3	1.59 [0.11x0.09]	2.61	2.30		DR 17
11	0.34 [0.11x0.06]	0.48	0.50		West SW of DR21
12	1.63 [0.11x0.09]	2.60	2.20		"
16	0.55 [0.12x0.12]	0.82	0.72		"
26	0.34 [0.20x0.10]	0.48	0.44		"
29	0.54 [0.25x0.13]	1.10	0.62		"
30	10.54 [0.15x0.10]	13.5	9.80		W75(N)
44	8.43 [0.14x0.11]	14.5	12.7		DR21 (OH)
46	17.90 [0.08x0.03]	18.4	15.8		DR21 f-f, maser (H2O)
48	3.72 [0.17x0.11]	9.4	7.8		DR21 (OH)-S
51	2.37 [0.24x0.03]	5.5	4.1		DR21 FIR2
53	1.60 [0.14x0.09]	4.3	2.7		North of DR21 FIR3
56	0.60 [0.12x0.08]	0.81	0.75		SE of DR21 47
58	2.73 [0.23x0.19]	2.40	1.64		IRAS 20375+4109
59	0.37 [0.12x0.05]	1.3	0.93		East of IRAS 20375+4109
60	0.56 [0.16x0.13]	1.00	0.78		East of IRAS 20375+4109
61	0.23 [0.12x0.09]	0.60	0.49		MSX 81.5168+0.01926
62	0.50 [0.18x0.12]	1.23	0.80		between 63 & IRAS 20375+4109
63	1.09 [0.08x0.05]	1.60	1.50		DR22
65	0.78 [0.16x0.12]	1.15	1.10		
66	0.25 [0.15x0.06]	0.63	0.76		
68	0.84 [0.10x0.10]	1.01	0.94		
69	1.28 [0.47x0.18]	1.12	1.20		
72	0.54 [0.28x0.13]	0.58	0.47		

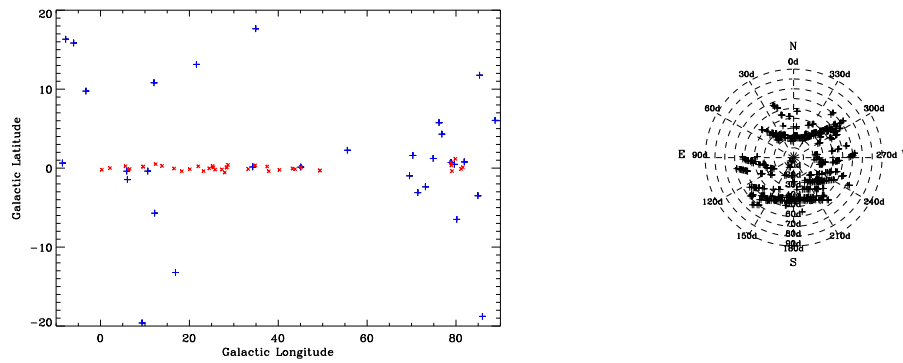
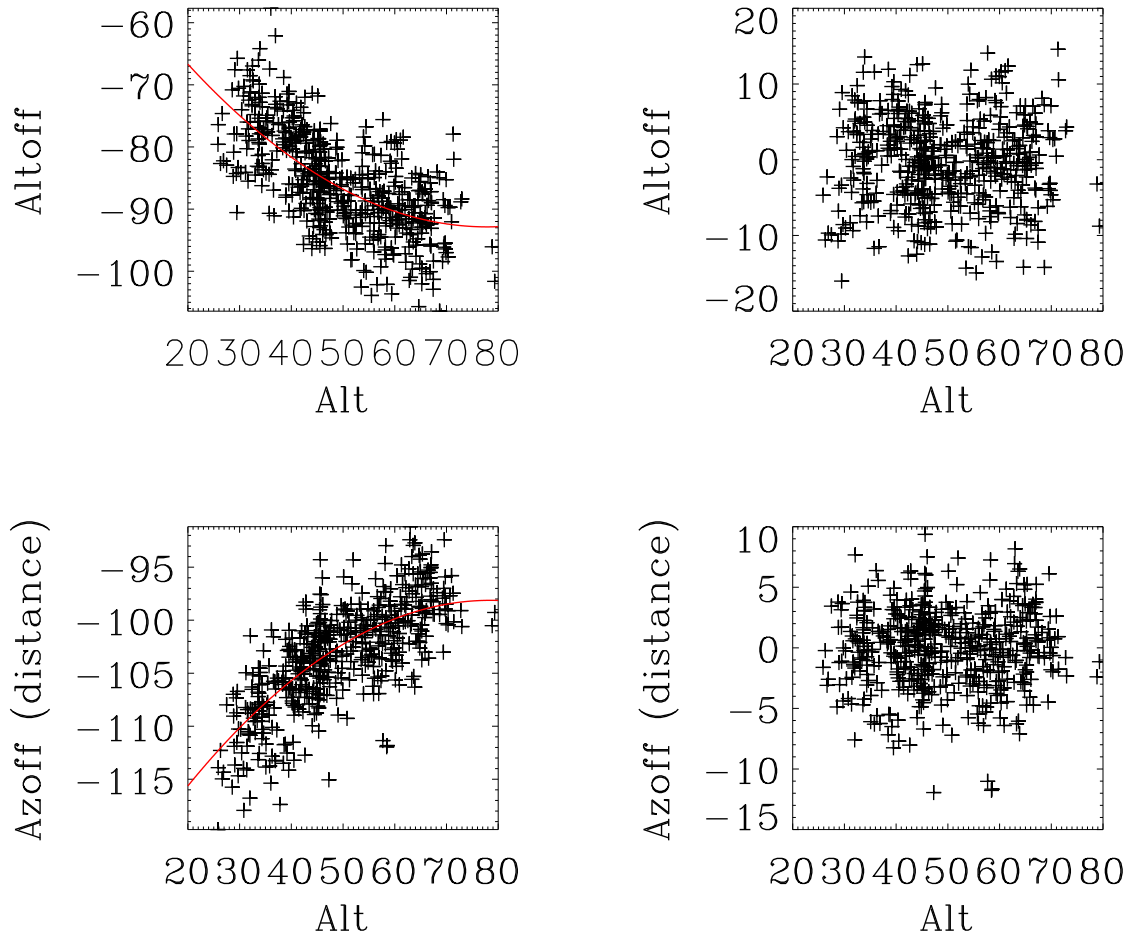
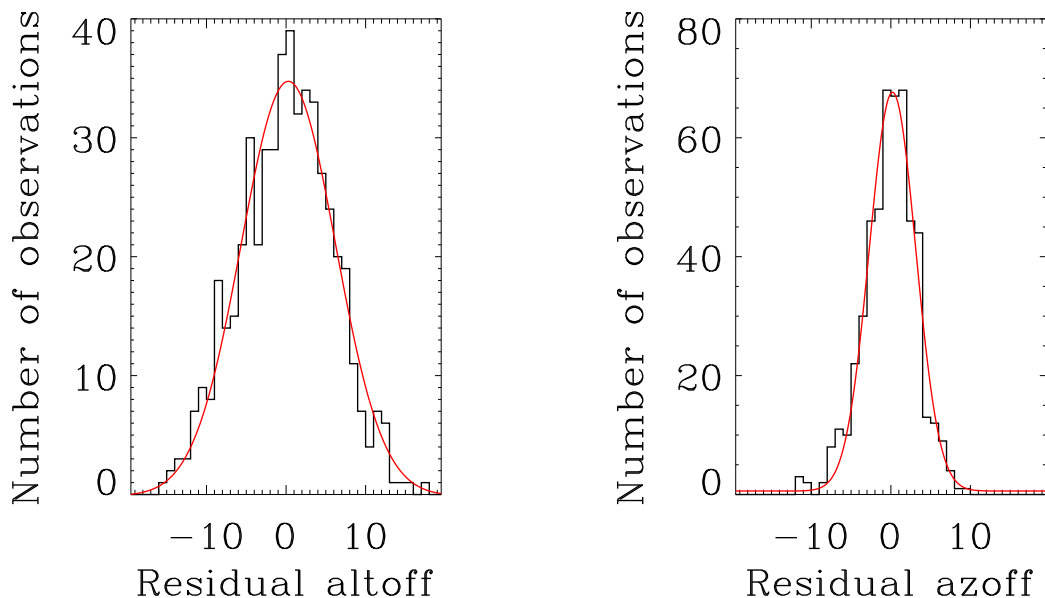


FIG. 7.— Left: The distribution of absolute reference sources (crosses) in the Galactic Plane (Appendix C). Also shown (crosses) are the locations of bright, isolated, compact sources for comparison with other surveys, as given in Appendix D. Right: The distribution of the pointing calibration sources across the local sky in Hawaii during July 2007 (epoch V) when the pointing model was constructed.



(a) The pointing model correction (left) and residuals (right) for Epoch V, from which the master reference images were derived for subsequent alignment. The red line indicates the fitted model. 510 pointing sources were included, and the final RMS was  $5.77''$  in altitude and  $3.21''$  in azimuth, or a total RMS offset of  $6.6''$ . No systematic offset with altitude was found.



(b) The residuals of the pointing model. The Gaussian fits have  $\sigma = 5.94, 2.92$  in altitude offset and azimuth offset respectively.

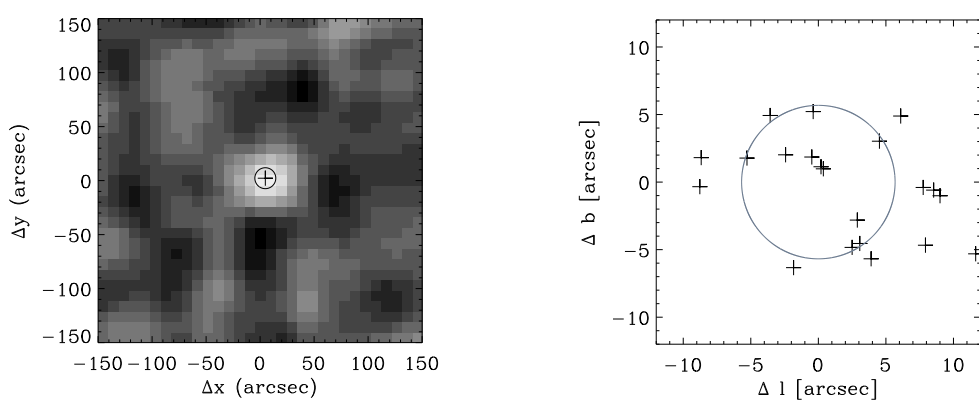
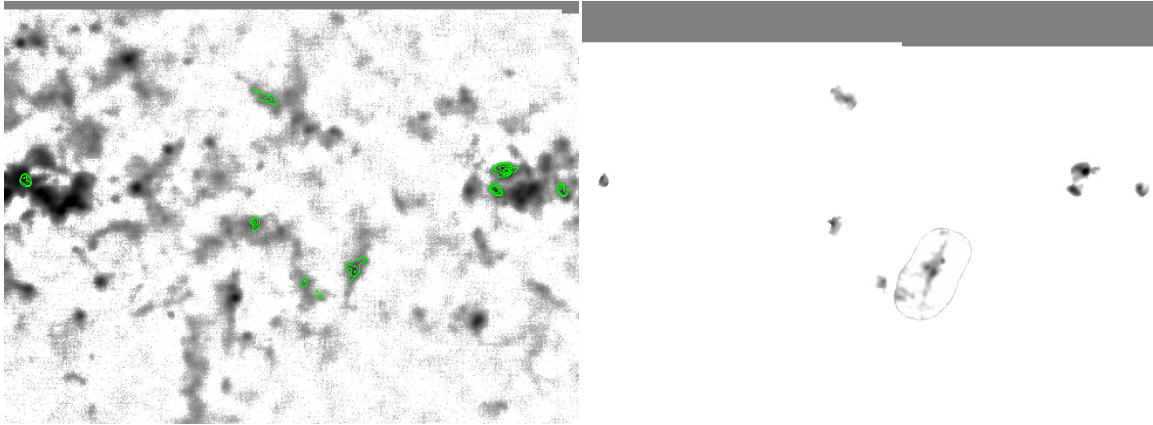


FIG. 9.— Comparing the Bolocam positions to those of the SCUBA Legacy Catalog.

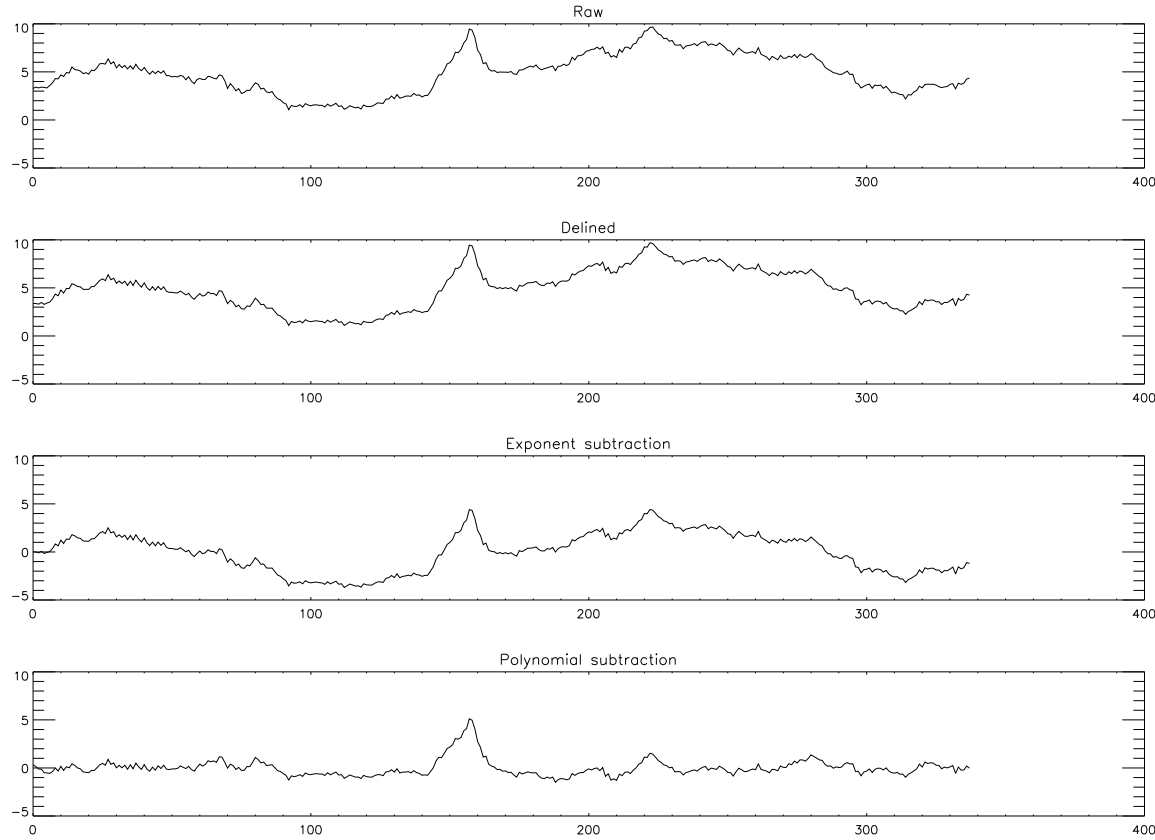


FIG. 10A.— An example of the change in the time series as iterative mapping proceeds. 1. Raw time series 2. After removal of residual 60Hz signal 3. Exponential decay function at scan turnarounds subtracted 4. A polynomial (with astrophysical source rejection) is fit to remove large-scale variations across the scan.

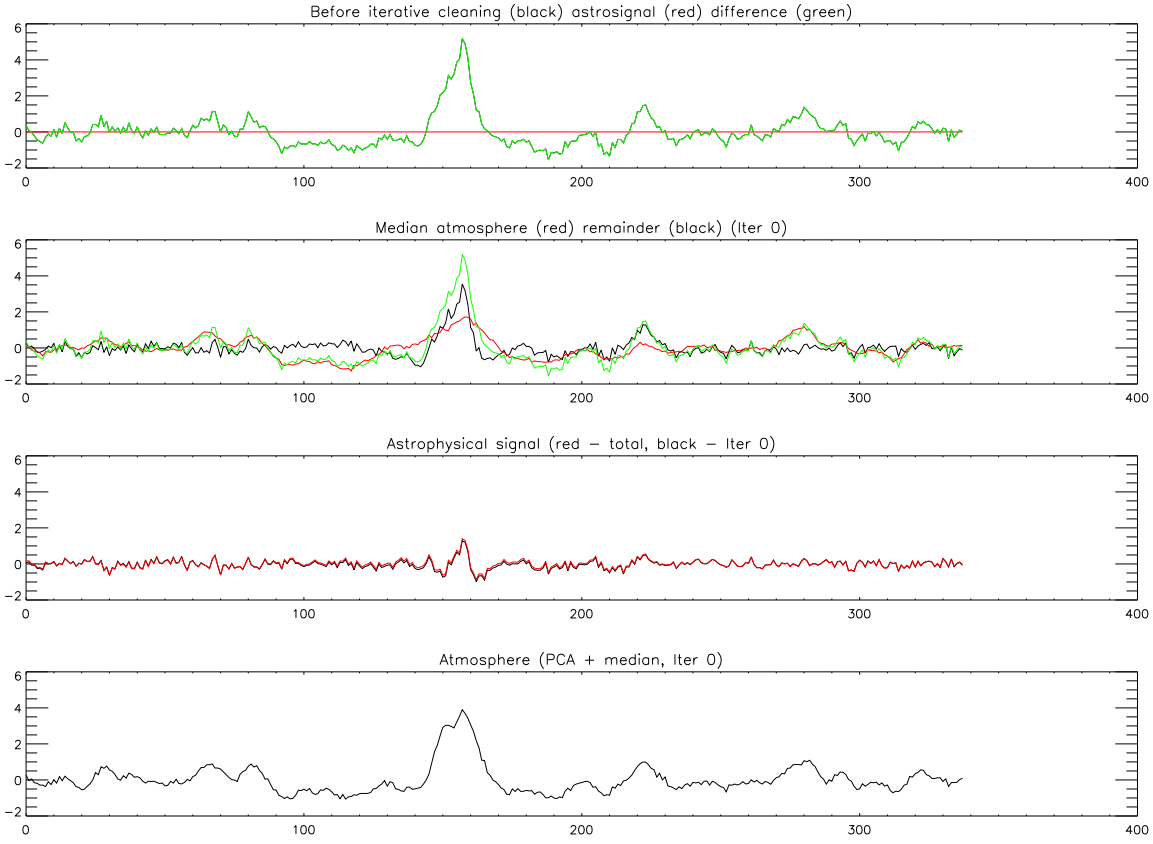


FIG. 11B.— Panel 1 is the same as panel 4 in the previous figure. Before the first cleaning, the raw data (black) and remainder data (green) are equal because there is no model. Panel 2 shows the median-atmosphere subtraction, which is the first-order correction. Panel 3 shows the astrophysical signal left over from the PCA selection. Panel 4 shows the total atmosphere model from PCA and median estimation

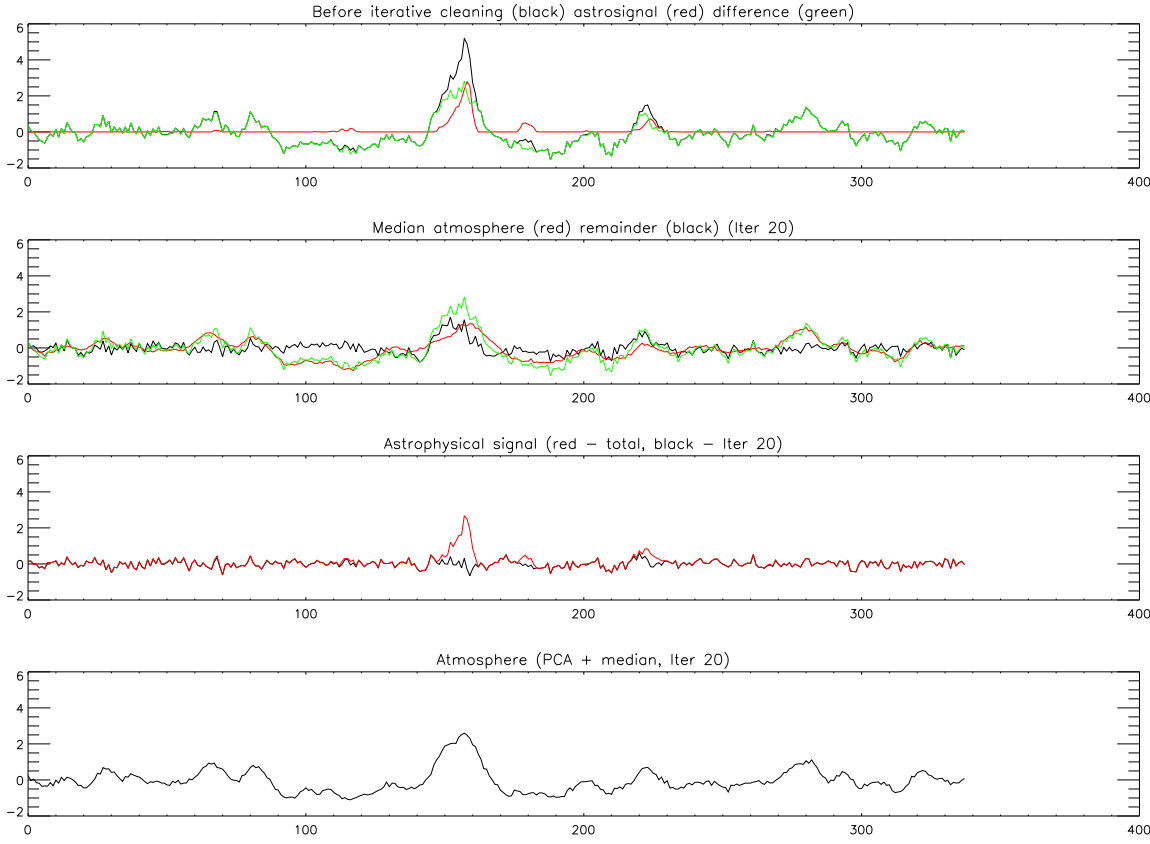


FIG. 12c.— Same as previous figure, except after 20 iterations. Panel 1 - The deconvolved astrophysical map is returned to a timestream (red) and subtracted from the 'raw' data (black). Panel 2 - The median of the remainder (green) is subtracted as the first atmosphere estimation Panel 3 - The cumulative astrophysical model (red) and the additional astrophysical signal from iteration 20 (black) Panel 4 - The atmosphere signal after 20 iterations

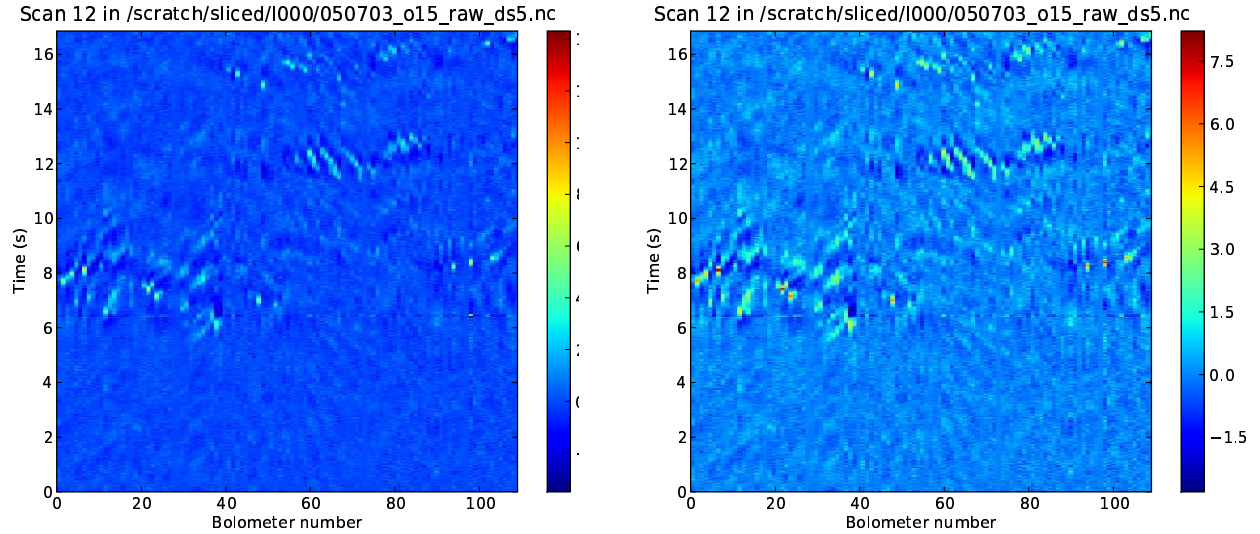


FIG. 13A.— An illustration of the flagging process using the waterfall plot. Left: The glitch apparent at middle right (bolometer 98, around 6.2s) is the same one whose time series is shown in (b). Because of the PCA subtraction, the effect of the glitch also propagates over the other bolometers, appearing as a horizontal stripe. Right: The same data displayed with the time point including the glitch flagged out and rescaled

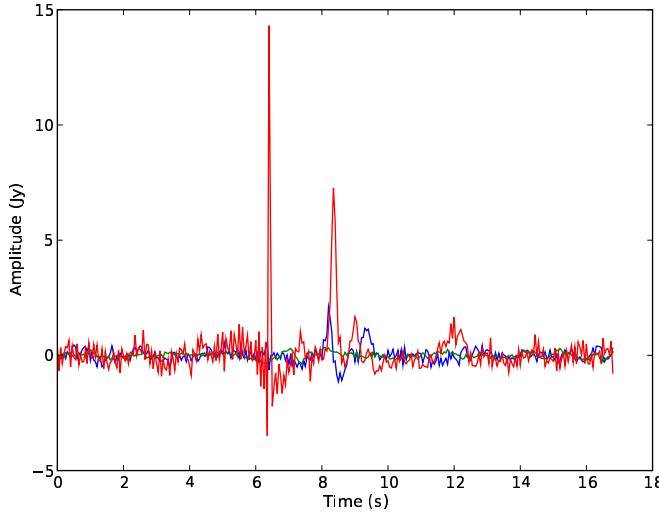


FIG. 14B.— An illustration of a “glitch” in a single bolometer timestream (red) due to a cosmic ray strike. Note the acausal ringing due to the application of the downsampling filter. The time series for a physically adjacent bolometer is shown in blue, and a bolometer which does not pass over the source in green. The PCA atmosphere estimation has already been subtracted from the data.

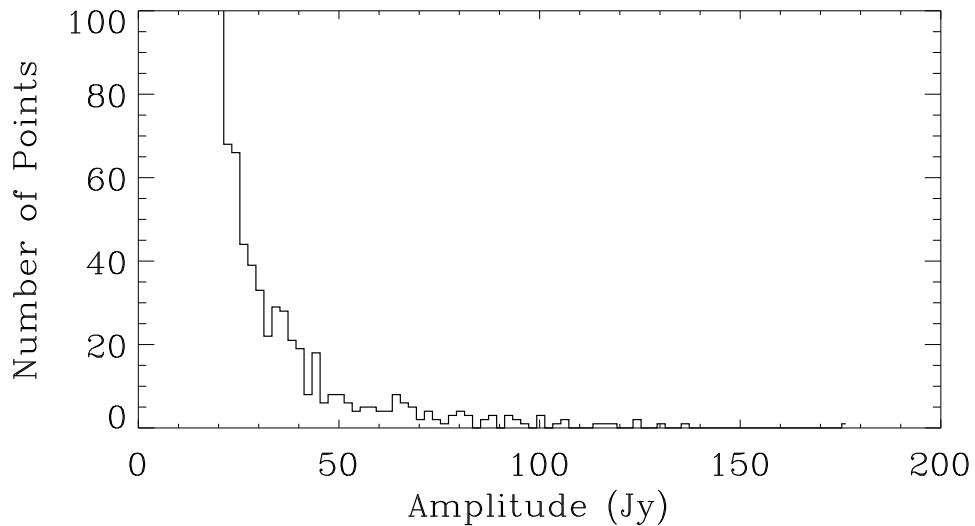


FIG. 15.— The distribution of glitch amplitudes flagged and removed from the data in the  $l=111$  field. Glitches below the detection threshold may contribute to the overall noise. Each data point represents .1s of integration time.

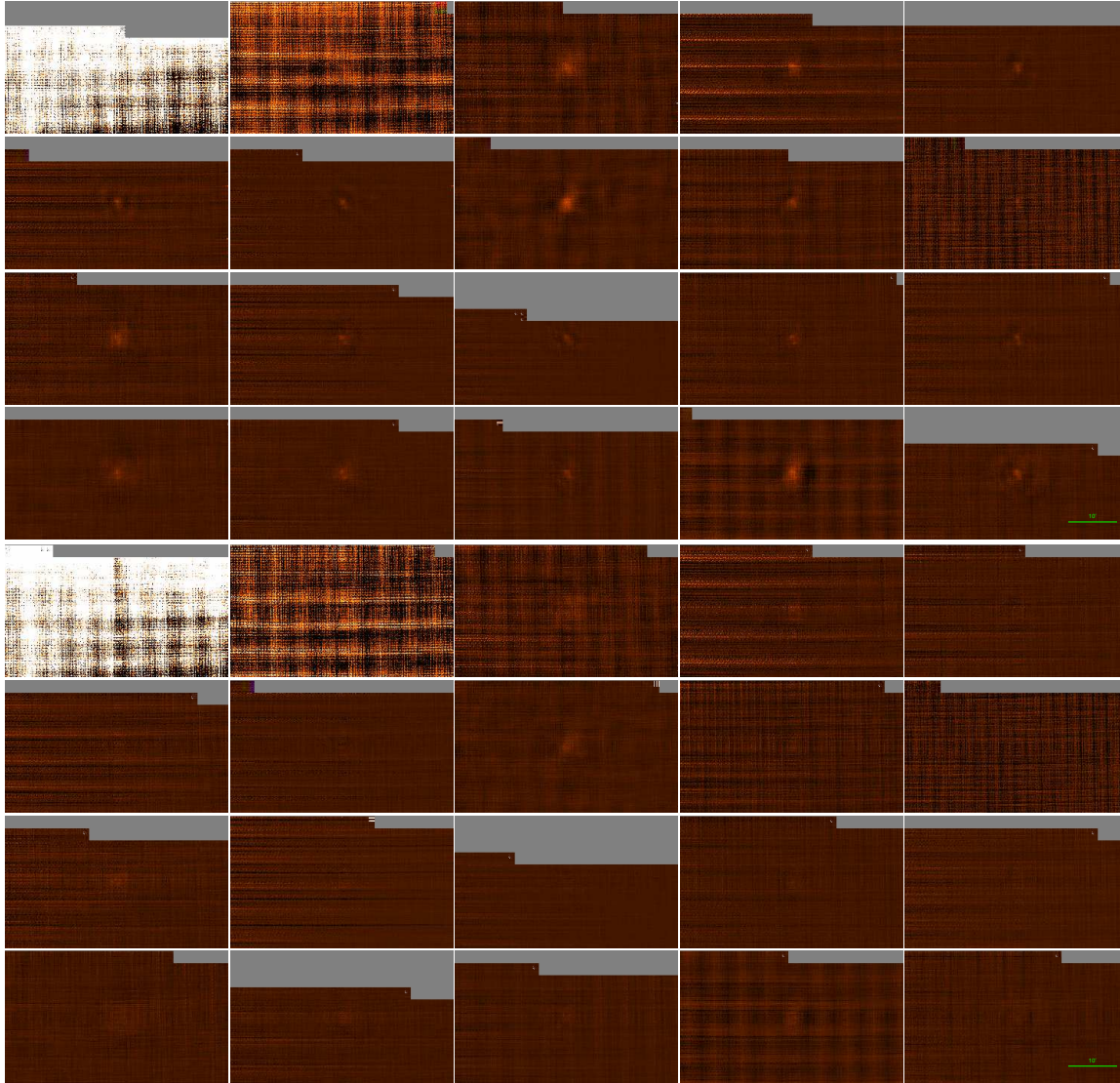


FIG. 16.— Selected images to illustrate the PCA process. The displays are in Galactic coordinates with a color range from  $-.1$  to  $1.0 \text{ Jy beam}^{-1}$ . *Top 4 rows*: a grid of maps of each of the first 20 PCA components displayed at the same scale. It is clear that NCG 7538, the object imaged, has emission in each component. There are varying levels of noise in each component, with the first and second being the most obvious atmospheric components. Most of the other noise components are probably detector noise correlated among a subset of the bolometers. The streaks are residuals of the scan-turnaround noise that was not removed by the exponential model fit. *Bottom 4 rows*: The same figure, but after 20 iterations. The figure is the breakdown of the atmosphere remainder (i.e. the raw data minus the astrophysical model) into eigenfunctions. Very little astrophysical flux remains at any level of correlation, though there is some at large (few arcminute) scales.

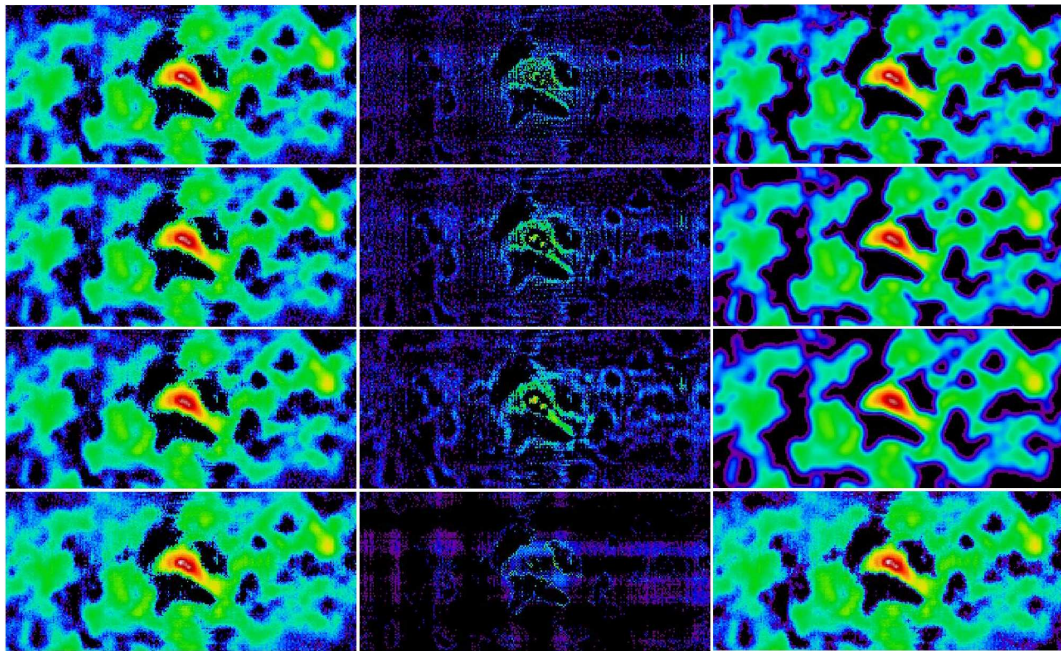


FIG. 17.— The effect of deconvolution on the iterative process can be seen in its effect on the residuals in these images of Sgr B2, all displayed at the same scale. From left to right: map, residual, model. Top to bottom kernel size: 14.4'', 21.6'', 31.2'', 7.2''. The final version of the pipeline uses 14.4'', which has the result of leaving no flux in the residual at the location of Sgr B2, and does not “dig a hole” in the residual map, as the 7.2'' kernel does. The 7.2'' kernel also lacks the noise-rejection features of the larger kernels, as can be seen in the last panel.

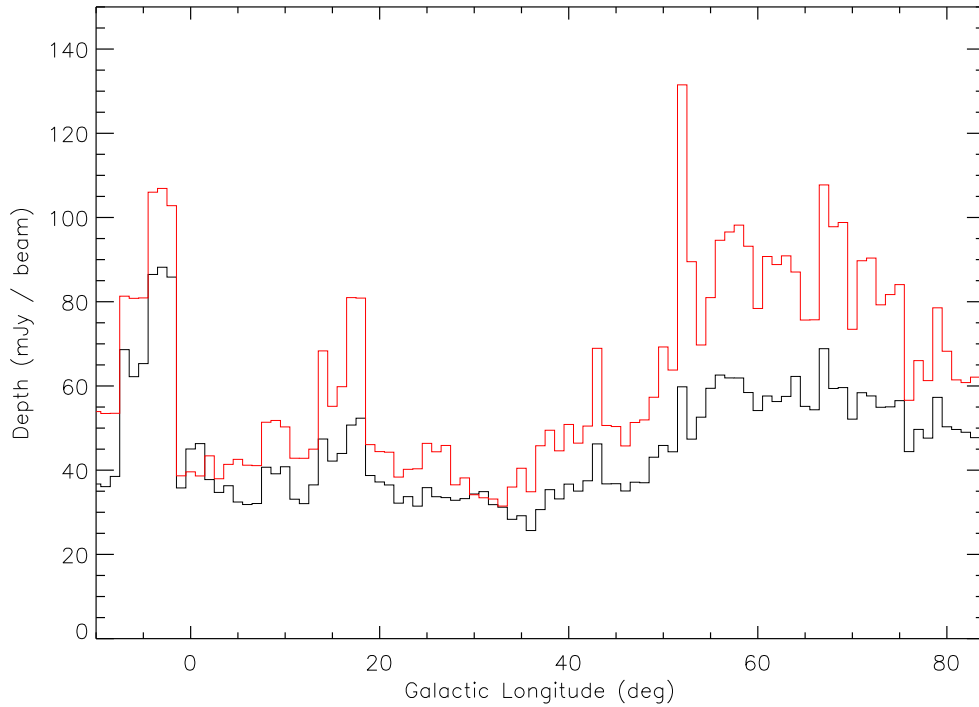


FIG. 18.— The depth of the BGPS in the first quadrant as a function of Galactic longitude. The black histogram plots the standard deviation as a function of longitude binned in  $0.9^\circ \times 0.9^\circ$  degree blocks (to avoid high-noise regions at scan edges) centered on  $b = 0$  for the error maps  $E$ . Red is similar, but the estimator is  $\text{median}(1/\sqrt{\text{weight map}})$ .

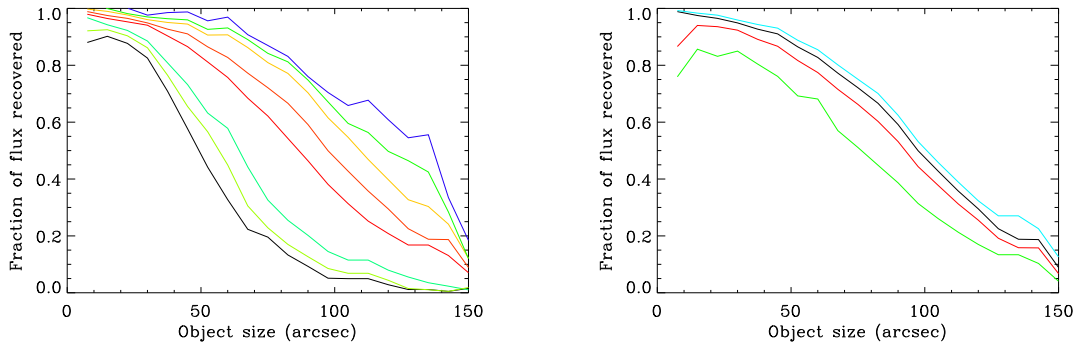


FIG. 19.— The fractional flux recovered as a function of source size for well-separated Gaussian sources with FWHM as indicated. *Left:* 3 (blue), 7 (green), 10 (yellow), 13 (orange), 16 (red), 21 (teal), 26 (lime), 31 (black) PCA components subtracted. Note that flux recovery drops to 50% at  $120''$  for the 13 PCA component cleaning used in the released data. The 3 and 7 PCA cases show bumps because atmospheric noise is still present at large scales. The  $>100\%$  recovery for simulated sources smaller than the deconvolution kernel is a side-effect; since the deconvolution kernel is smaller than the beam, no real astrophysical source should ever be smaller than the kernel. *Right:*  $7.2''$ (cyan),  $14.4''$ (black),  $21.6''$ (red),  $31.2''$ (green) deconvolution kernel for 13 PCA components subtracted. It is clear that the larger deconvolution kernels generate spurious signal at smaller scales, but the flux recovery is very close to 1 at the beam size ( $33''$ )

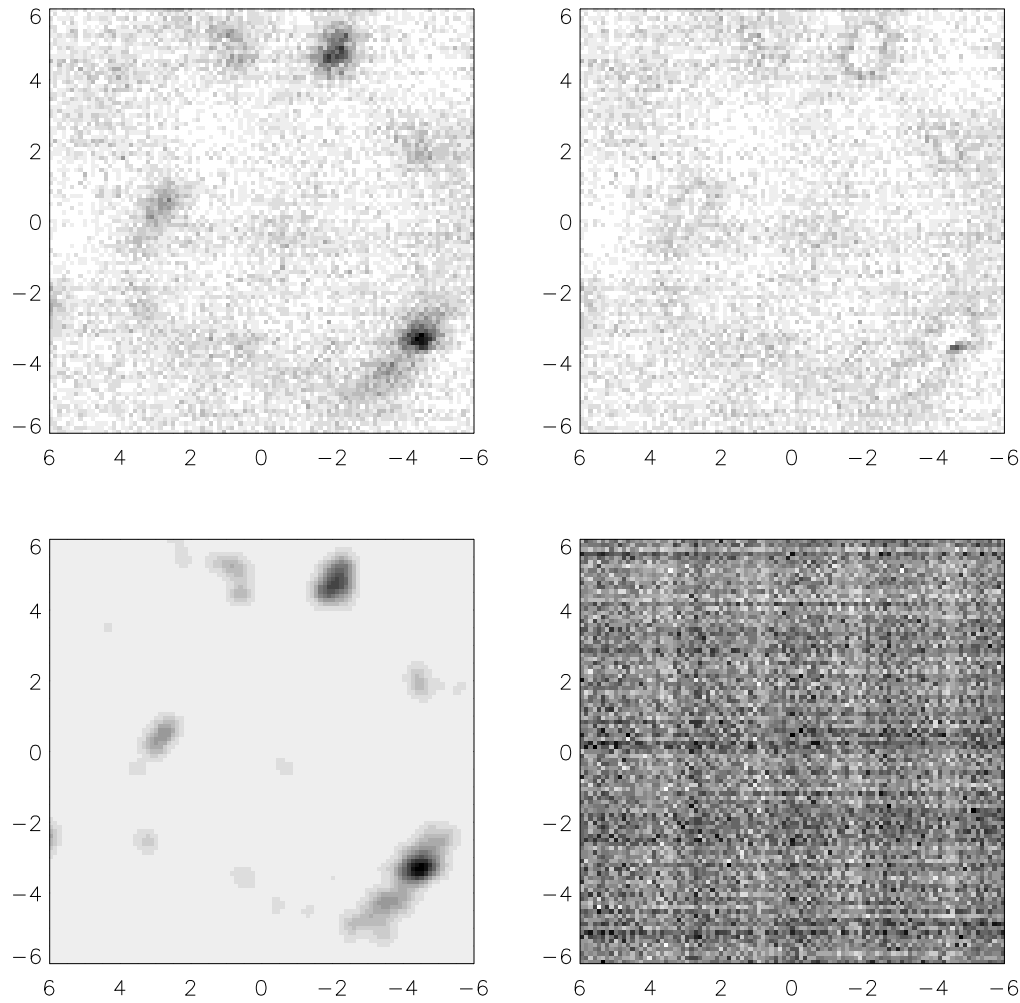
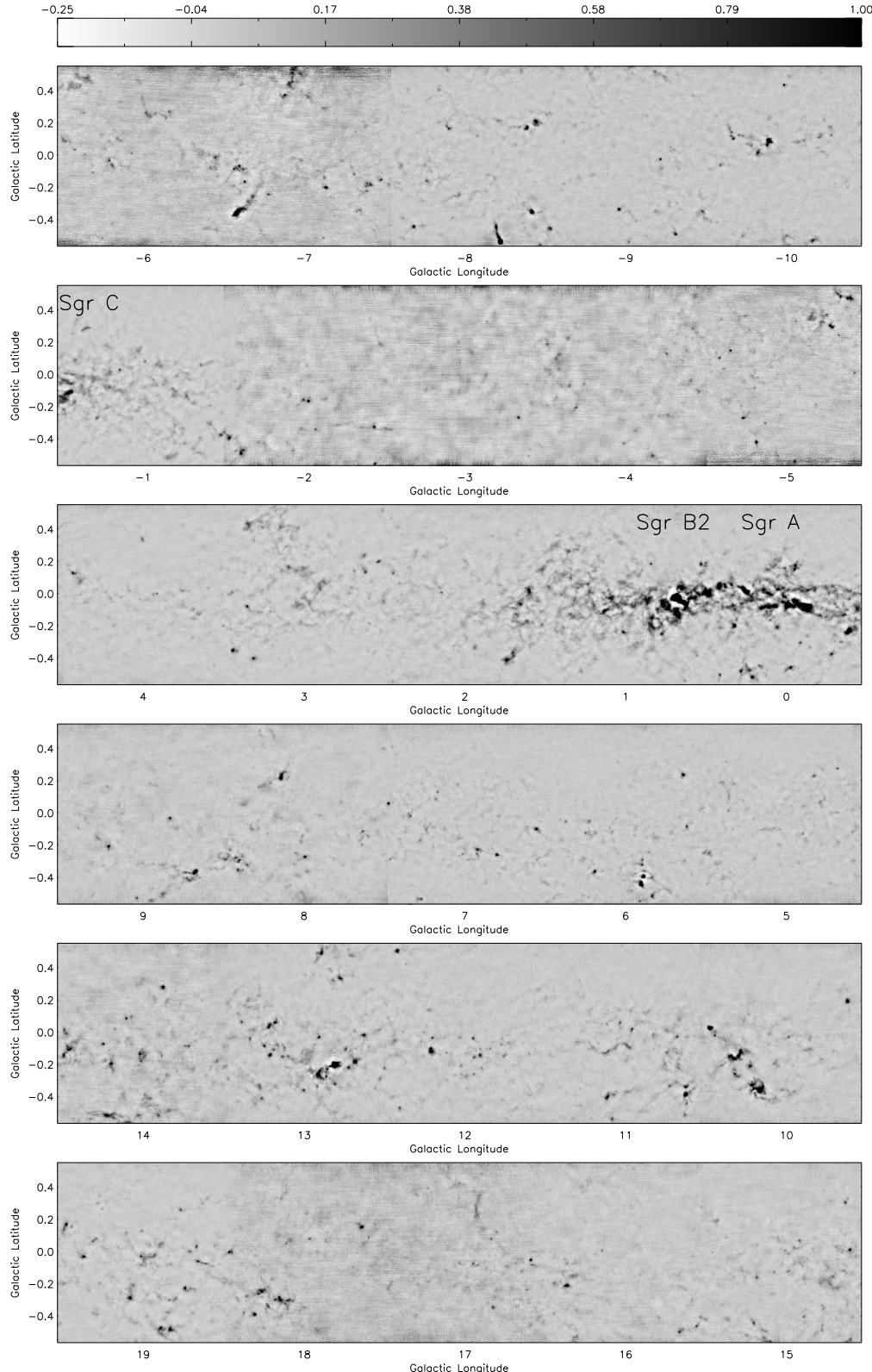


FIG. 20.— Examples of four of the image types being released. Axes are offsets in arcminutes. See section 9. Top left: Map. Top right: Residual. Bottom left: Deconvolved. Bottom right: Weight

FIG. 21.— Images from the BGPS.

FIG. 21B.—  $l = -10.5$  to  $l = 19.5$  Units are  $\text{Jy beam}^{-1}$ . The brightest sources, e.g. Sgr B2, Sgr A, and sources near  $l = 10$  and  $l = 13$ , appear to be saturated, but this is only a display artifact. The noise is more pronounced from  $l = -7$  to  $l = -2$  because this region was observed less.

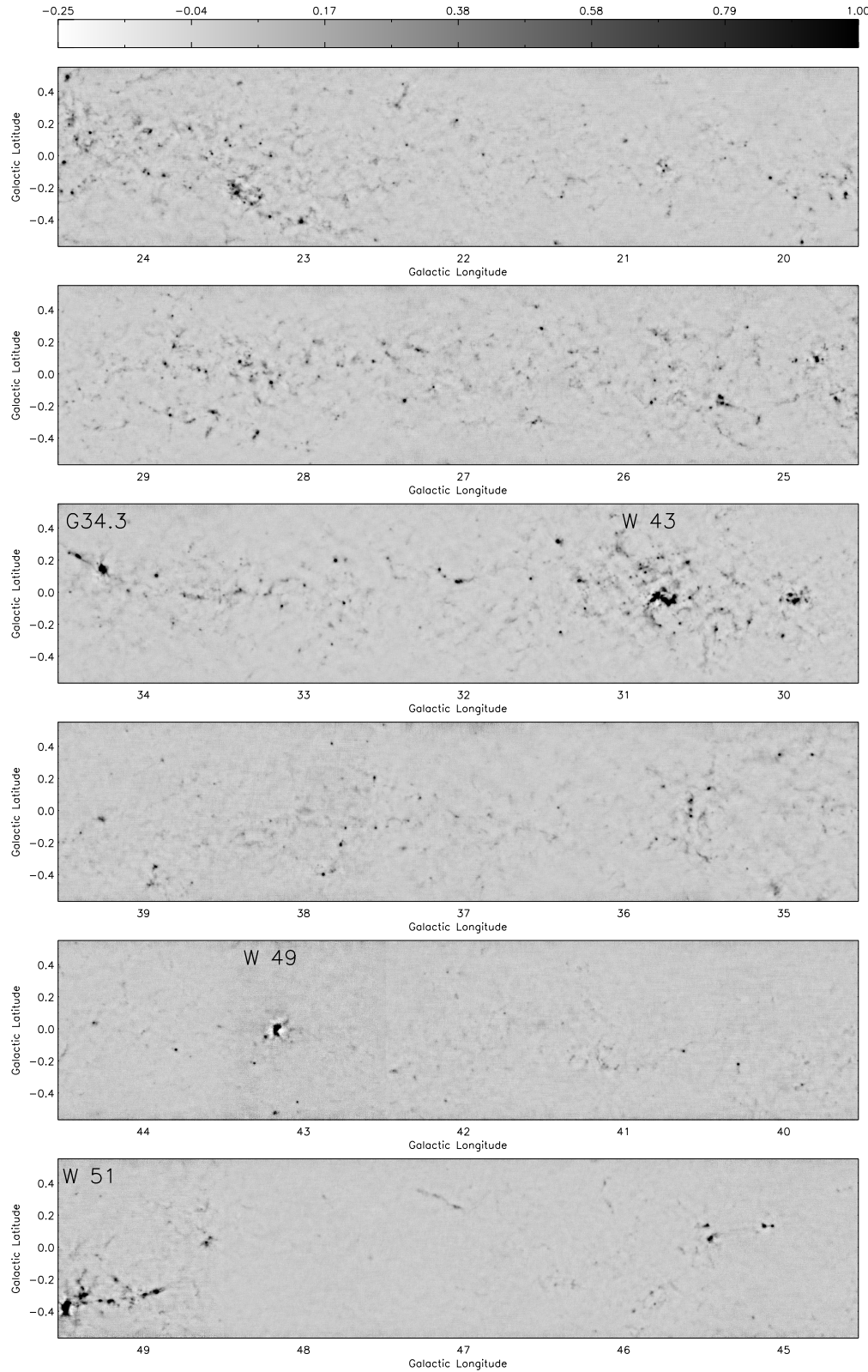


FIG. 21.—  $l = 19.5$  to  $l = 49.5$ . Units are Jy beam<sup>-1</sup>. G34.3+0.15, W 51, W 43, W 49, and M 17 appear to be saturated, but this is only a display artifact. The  $20 < l < 40$  region through the 4–8 kpc molecular ring and approximately the termination of the galactic bar is particularly rich in clumps.

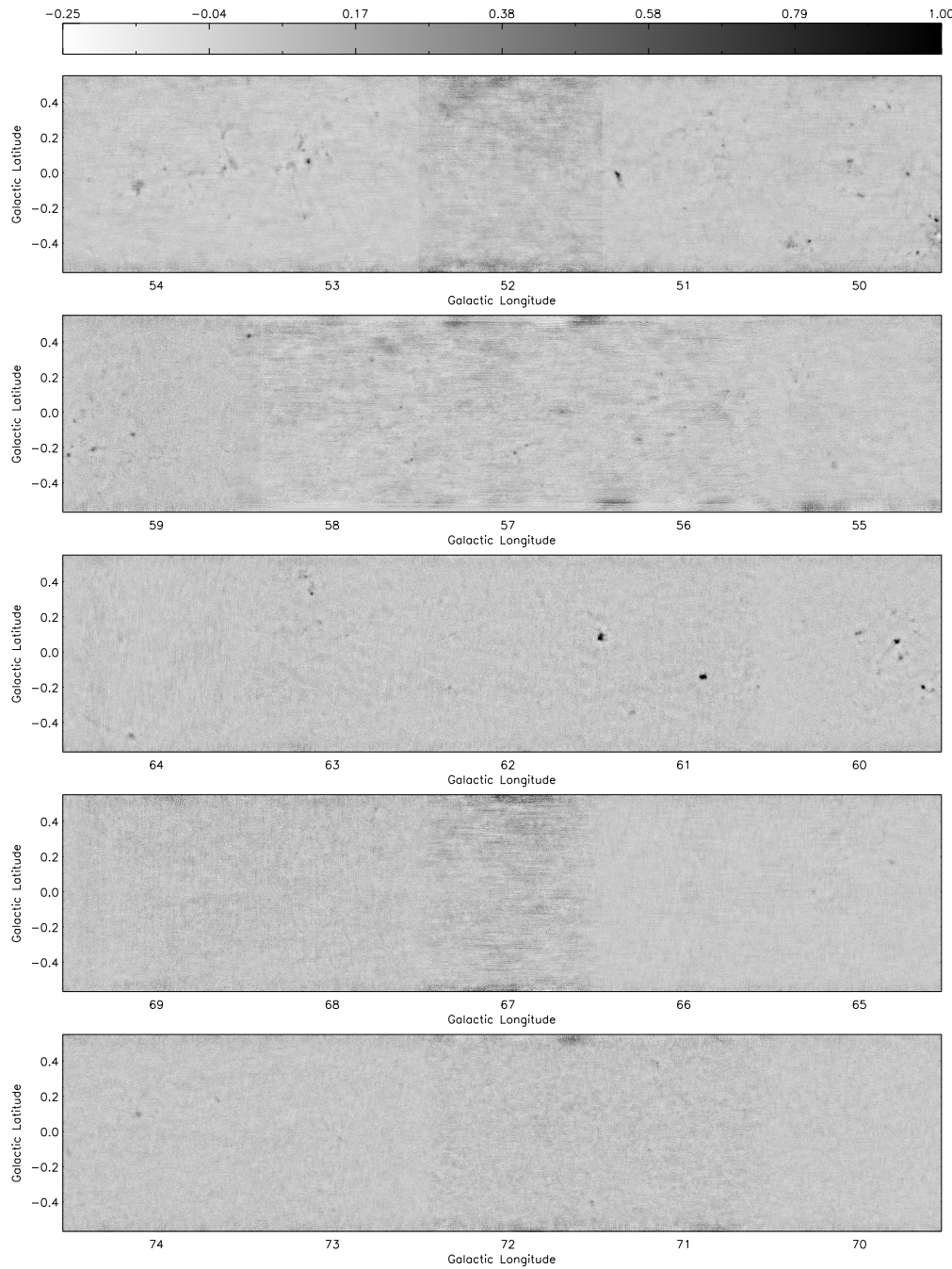


FIG. 21.—  $l = 49.5$  to  $l = 74.5$ . In comparison to the inner galaxy, the  $65 < l < 75$  has a very sparse population of faint clumps

-0.25      -0.04      0.17      0.38      0.58      0.79      1.00

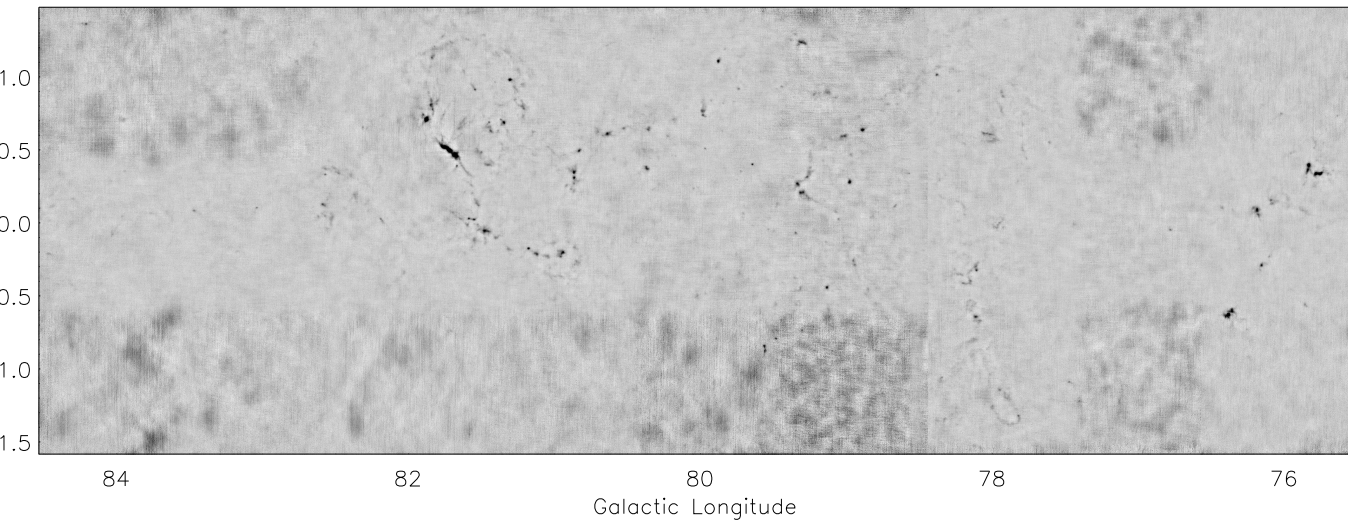



FIG. 21.— The Cygnus Arm. Note that coverage in  $b$  is extended to  $\pm 1.5$  deg. The large scale ‘peanut’ shape including DR21 is suggestive of a large wind-blown bubble, although.... [John: fill in discussion here or we’ll remove it]. See section 4.1 for a comparison with the Motte et al. (2007) IRAM study of this region.

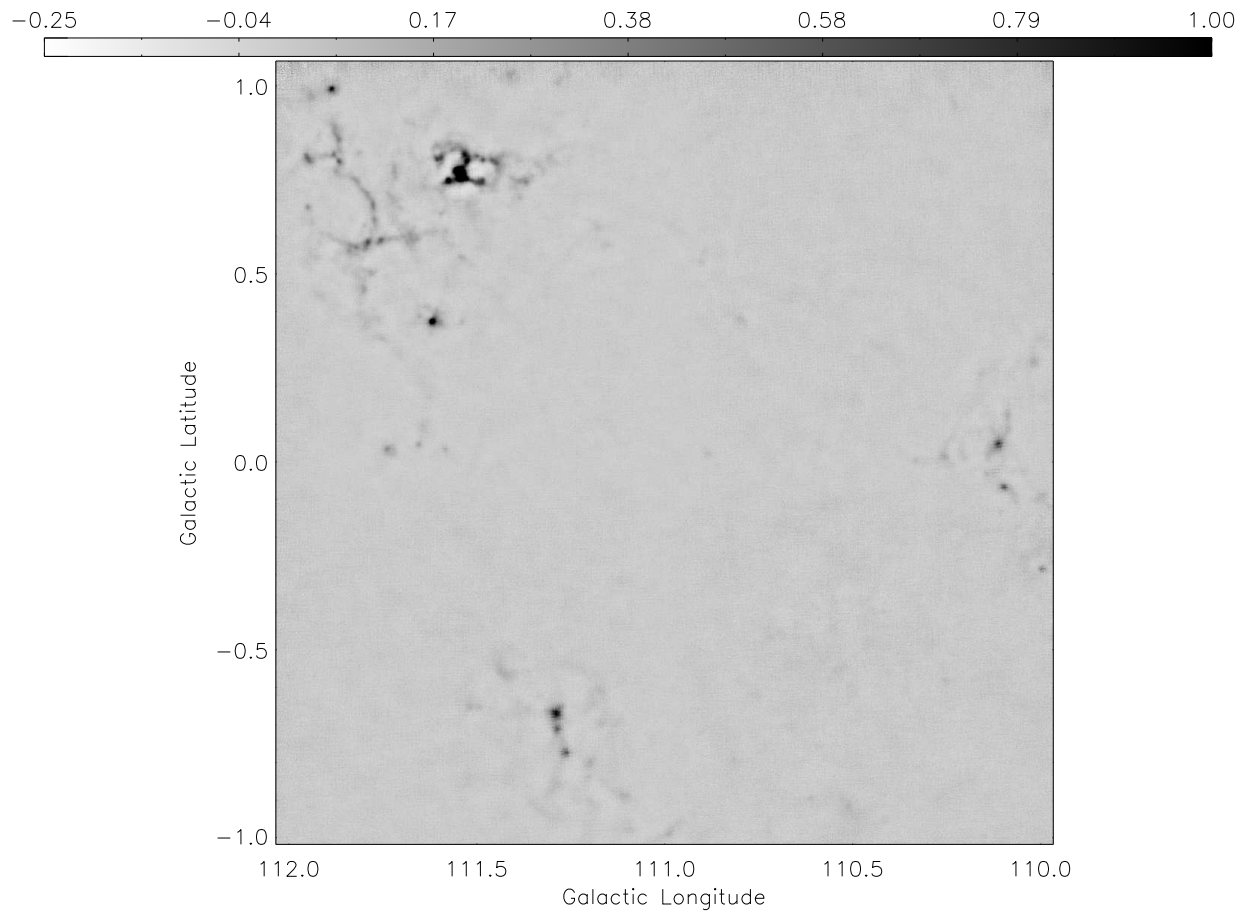


FIG. 21.— Cloud complexes centered at  $l = 111$  in the Perseus Arm. The NGC 7538 complex is in the upper-left.

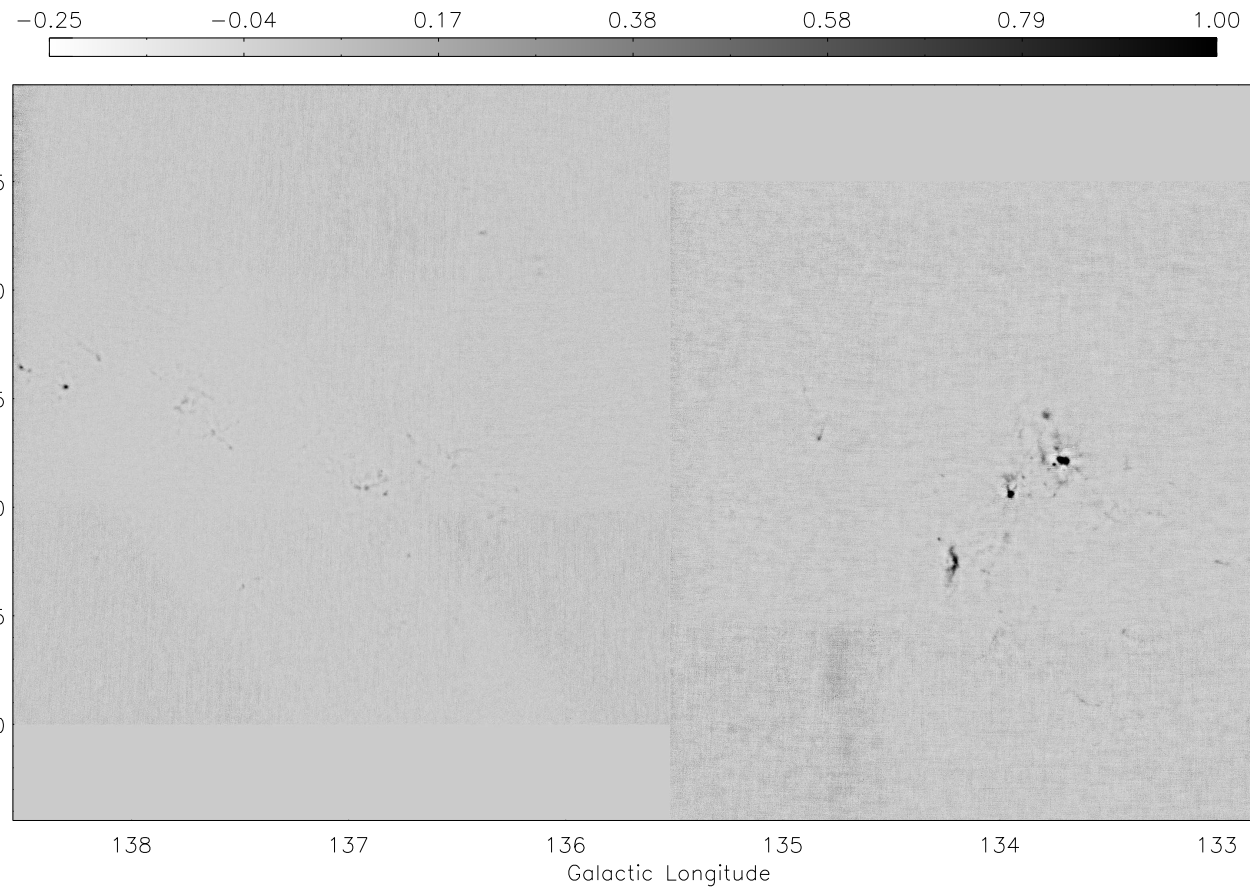


FIG. 21.— W3/4/5. The W3(OH)/W3 Main complex is the bright source on the right side of the image. W5 has one scan performed in RA/Dec instead of Galactic coordinates and so has non-uniform noise properties in each square degree

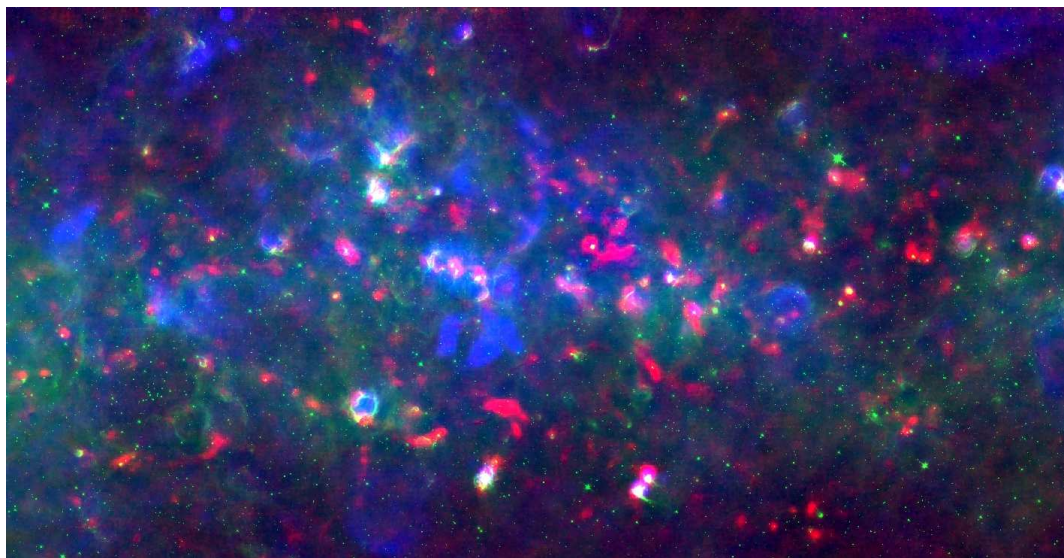


FIG. 22.— An RGB image of a portion of the Galactic Plane, combining Bolocam (red), VGPS 20 cm continuum (green) and Spitzer GLIMPSE 8  $\mu\text{m}$  (blue).

## REFERENCES

- Bally, J. et al. 2009, ApJ, in prep
- Battersby, M. et al. 2009, ApJ, in prep
- Benjamin, R. A. et al. 2003, PASP, 115, 953
- Beuther, H. et al. 2004, ApJ, 616, L31
- Cotton, W. D. et al. 2009, ArXiv e-prints
- Cyganowski, C. J., Brogan, C. L., & Hunter, T. R. 2007, AJ, 134, 346
- Dame, T. M., Hartmann, D., & Thaddeus, P. 2001, ApJ, 547, 792
- Di Francesco, J., Johnstone, D., Kirk, H., MacKenzie, T., & Ledwosinska, E. 2008, ApJS, 175, 277
- Enoch, M. L., Evans, II, N. J., Sargent, A. I., Glenn, J., Rosolowsky, E., & Myers, P. 2008, ArXiv e-prints, 805
- Enoch, M. L., Glenn, J., Evans, II, N. J., Sargent, A. I., Young, K. E., & Huard, T. L. 2007, ApJ, 666, 982
- Enoch, M. L. et al. 2006, ApJ, 638, 293
- Evans, N. J. et al. 2009, ApJS, 181, 321
- Glenn, J. et al. 2003, in Proc. SPIE, Vol. 4855, Millimeter and Submillimeter Detectors for Astronomy, 30
- Griffin, M. J. & Orton, G. S. 1993, Icarus, 105, 537
- Haig, D. J. et al. 2004, in Proc. SPIE, Vol. 5498, Millimeter and Submillimeter Detectors for Astronomy II., ed. J. Zmuidzinas, W. S. Holland, & S. Withington, 78
- Holland, W. S. et al. 1999, MNRAS, 303, 659
- Hollis, J. M., Dorband, J. E., & Yusef-Zadeh, F. 1992, ApJ, 386, 293
- Jackson, J. M. et al. 2006, ApJS, 163, 145
- Johnstone, D. & Bally, J. 1999, ApJ, 510, L49
- . 2006, ApJ, 653, 383
- Kauffmann, J., Bertoldi, F., Bourke, T. L., Evans, II, N. J., & Lee, C. W. 2008, A&A, 487, 993
- Kovács, A. 2008, in Presented at the Society of Photo-Optical Instrumentation Engineers (SPIE) Conference, Vol. 7020, Society of Photo-Optical Instrumentation Engineers (SPIE) Conference Series
- Lada, E. A., Bally, J., & Stark, A. A. 1991, ApJ, 368, 432
- Laurent, G. T. et al. 2005, ApJ, 623, 742
- McKee, C. F. & Ostriker, E. C. 2007, ARA&A, 45, 565
- Motte, F., Bontemps, S., Schilke, P., Schneider, N., Menten, K. M., & Broguière, D. 2007, A&A, 476, 1243
- Mueller, K. E., Shirley, Y. L., Evans, II, N. J., & Jacobson, H. R. 2002, ApJS, 143, 469
- Nordhaus, M. et al. 2009, ApJ, in prep
- Nummelin, A., Bergman, P., Hjalmarson, A., Friberg, P., Irvine, W. M., Millar, T. J., Ohishi, M., & Saito, S. 1998, ApJS, 117, 427
- Orton, G. S., Griffin, M. J., Ade, P. A. R., Nolt, I. G., & Radostitz, J. V. 1986, Icarus, 67, 289
- Ossenkopf, V. & Henning, T. 1994, A&A, 291, 943
- Pohl, M., Englmaier, P., & Bissantz, N. 2008, ApJ, 677, 283
- Reid, M. J. et al. 2009, ArXiv e-prints
- Rosolowsky, E. et al. 2009, ApJ, in prep
- Sayers, J. et al. 2009a, ApJ, submitted
- . 2009b, ApJ, 690, 1597
- Schlingman, W. et al. 2009, ApJ, in prep
- Schuller, F. et al. 2009, ArXiv e-prints
- Simon, R., Rathborne, J. M., Shah, R. Y., Jackson, J. M., & Chambers, E. T. 2006, ApJ, 653, 1325
- Testi, L. & Sargent, A. I. 1998, ApJ, 508, L91
- van Dishoeck, E. F. & Blake, G. A. 1998, ARA&A, 36, 317
- Williams, J. P., Blitz, L., & McKee, C. F. 2000, Protostars and Planets IV, 97
- Yoshida, H. & Phillips, T. G. 2005, in IAU Symposium, Vol. 235, IAU Symposium, 245P-+